Final Report:

Study of Plasma Liner Driven Magnetized Target Fusion via Advanced Simulations

Office of Fusion Energy Sciences, U.S. Department of Energy
grant DE-SC0004524

PI: Roman Samulyak[1,2], Co-PI: Paul Parks[3]
[1]*Department of Applied Mathematics and Statistics,*
Stony Brook University, Stony Brook, NY 11794
[2]*Computational Science Center,*
Brookhaven National Laboratory, Upton, NY 11973
[3]*General Atomics, P.O. Box 85608,*
San Diego, California 92186-5608

Contents

1 Spherically Symmetric Simulations of Deuterium and Heavy-Z Liners and Compression of Targets

1.1 Summary

In this Section, spherically symmetric simulations of the implosion of plasma liners and compression of plasma targets in the concept of the Plasma Jet driven Magneto Inertial Fusion (PJMIF) have been performed using the method of front tracking. The cases of single deuterium and xenon liners and double layer deuterium - xenon liners compressing various deuterium-tritium targets have been investigated, optimized for maximum fusion energy gains, and compared with theoretical predictions and scaling laws. In agreement with the theory, the fusion gain was significantly below unity for deuterium - tritium targets compressed by Mach 60 deuterium liners. In the most optimal setup for a given chamber size that contained a target with the initial radius of 20 cm compressed by 10 cm thick, Mach 60 xenon liner, the target ignition and fusion energy gain of 10 was achieved. Simulations also showed that composite deuterium - xenon liners reduce the energy gain due to lower target compression rates. The effect of heating of targets by alpha particles on the fusion energy gain has also been investigated. This Section is based on [1]

1.2 Numerical method and the problem setup

FronTier is a computational package for the direct numerical simulation of multiphase flows based on the method of front tracking developed at Stony Brook University in collaboration with LANL and BNL [5, 6]. An important and unique feature of this package is its robust ability to track dynamically moving fronts or material interfaces.

Front tracking is a hybrid Lagrangian - Eulerian method. FronTier represents interfaces as lower dimensional Lagrangian meshes moving through a volume filling Eulerian grid. FronTier can evolve and resolve topological changes of a large number of interfaces in 2D and 3D spaces. The dynamics of interfaces is described by the theory of the Riemann problem for systems of conservation laws which is the problem of finding self-similar solutions to the systems of conservation laws with discontinuity of initial conditions at one point. The main advantage of explicitly tracked interfaces is the absence (or large reduction) of numerical diffusion. Explicit geometrical interfaces also enable us to describe accurately physics processes occurring at material interfaces (for instance phase transitions), and apply different physics and numerical approximations in regions separated by interfaces. The last feature is especially important for the simulation of complex multiscale and multiphysics processes. Currently FronTier supports compressible and incompressible Navier-Stokes equations with phase transitions, MHD equations in the low magnetic Reynolds number approximation, and oil reservoir equations. The FronTier code has been used on various supercomputers for the simulation of complex multiphase systems of theoretical (turbulent fluid mixing) and applied (liquid accelerator targets, fuel jets, pellet fueling of tokamaks, etc.) importance.

FronTier geometrical and physics features make it a very effective tool for the simulation of converging supersonic plasma jets, the formation of an imploding liner, and the compression of a magnetized plasma target in PJMIF devices. In 1D spherically symmetric simulations presented in this paper, each material interface is a single tracked point that eliminates the

numerical diffusion caused by strong gradients of fields.

1.3 Comparison of simulations with theoretical predictions

In this section, we perform detailed comparison of numerical simulations with theoretical predictions of [8]. The main formulas are summarized below.

The fusion energy gain was obtained in simulations using the following approach. At each time step, the production of fusion neutrons was calculated for each computational cell of the target based on the thermodynamic state of the target and the fusion reactivity [7]

$$< \sigma v >= c_1 \theta(T) \sqrt{\frac{[BG^2/(4\theta(T))]^{1/3}}{D\,T^3}} \exp\left[-3\left[BG^3/(4\theta(T))\right]^{1/3}\right], \tag{1}$$

where

$$\theta(T) = \frac{T}{1 - \frac{T(c_2+T(c_4+Tc_6))}{1+T(c_3+T(c_5+Tc_7))}}.$$

Here the temperature T is in keV units, the dimension of the fusion reactivity is cm^3/s, and coefficients have the following numerical values $c_1 = 1.17302 \times 10^{-9}$, $c_2 = 0.0151361$, $c_3 = 0.0751886$, $c_4 = 0.00460643$, $c_5 = 0.0135$, $c_6 = -1.0675 \times 10^{-4}$, $c_7 = 1.366 \times 10^{-5}$, $BG = 34.3827$, $D = 1.124656 \times 10^6$. The neutron production was integrated in the target volume and time to obtain the total fusion energy

$$E_{\text{fusion}} = (e_{\text{neutron}} + e_\alpha) \int_{t_0}^{\infty} \int\int\int_{V_{target}(t)} < \sigma v > \frac{n^2}{4}\, dV\, dt, \tag{2}$$

where n is the target number density, $e_{\text{neutron}} = 14.1$ MeV is the neutron energy and $e_\alpha = 3.5$ MeV is the alpha particle energy released in the process of fusion.

Finally, the fusion gain was obtained as

$$G_{\text{simulation}} = E_{\text{fusion}}/E_{\text{liner}}, \tag{3}$$

where

$$E_{\text{liner}} = E_{\text{kinetic}} + E_{\text{internal}} \simeq E_{\text{kinetic}}$$

is the total initial energy of the liner. Notice that (25) does not account for the efficiency of electromagnetic plasma guns that generate plasma jets. The efficiency of the plasma guns is not precisely known. We believe that it is currently in the range of 20% - 70% and can be increased in the future as the technology develops.

We will compare the simulated fusion energy gain (25) with theoretical estimates of [8] obtained as follows. If all the deuterium - tritium fuel in the target could be burned up, then the maximum (ideal) fusion energy gain would be 293 at the ignition temperature of 10 keV. The actual fusion energy gain is

$$G_{\text{theory}} = 293 f_b \eta_h. \tag{4}$$

In this expression, η_h is the hydrodynamic efficiency and f_b is the fuel burn up fraction coefficient

$$f_b =< \sigma v > n\tau_{dc}/2, \tag{5}$$

where n is the target number density and τ_{dc} is the deconfinement time defined as the time during which the pressure in the target decreases by the factor of two compared to the fully compressed state. The hydrodynamic efficiency is defined as the ratio of the internal energy of the compressed target to the initial energy of the liner,

$$\eta_h = \frac{E_{\text{target}}}{E_{\text{liner}}}, \tag{6}$$

where

$$E_{\text{target}} = \frac{PV}{\gamma - 1}.$$

According to [8], the hydrodynamic efficiency can be expressed as

$$\eta_h = \frac{R}{L} H\left(\gamma, M_{\text{liner}}\right), \tag{7}$$

where R is the compressed target radius, L is the initial thickness of the liner (the length of merging jets), and H is a function of the adiabatic gamma and the initial Mach number of the liner. $H = 1.23$ for $\gamma = 5/3$ and $M_{\text{liner}} = 60$. The deconfinement time was estimated in [8] as

$$\tau_{dc} \sim 2R/u_j \sim (R/c_{sc})(\rho_2/\rho)^{1/2}, \tag{8}$$

where u_j is the initial plasma jet (liner) velocity, ρ_2 and ρ are density values of the compressed liner and target (at the liner - target interface), correspondingly, and $c_{sc} = (2T_{ign}/m)^{1/2} = 8.78 \times 10^7\, cm/s$ is the thermonuclear sound speed. Replacing this value with the actual sound speed in the target $c = \sqrt{(}\gamma P/\rho)$, we obtain the deconfinement time as

$$\tau_{dc} \sim R(\rho_2/\gamma P)^{1/2}. \tag{9}$$

This formula predictions will be compared in this paper with computed values of the deconfinement time.

In this section, we study the liner - target setup suggested in [8]. A 15 cm thick deuterium liner implodes and compresses the plasma target. The initial inner radius of the liner is 60 cm, which corresponds to the merging radius of plasma jets forming the liner. The initial state of the liner is as follows: the density $\rho = 3.8 \times 10^{-5}\,\text{g/cm}^3 = 9.2 \times 10^{18}\,1/\text{cm}^3$, temperature $T = 0.0358\,\text{eV} = 415.4\,\text{K}$, pressure $P = 0.65\,\text{bar}$, velocity $v = 100\,\text{km/s}$, and the Mach number $M = 60$. The total energy stored in the liner is 164 MJ. The plasma target is initially 5 cm in radius, and its initial density, pressure, and temperature are $\rho = 8.3 \times 10^{-6}\,\text{g/cm}^3 = 2 \times 10^{18}\,1/\text{cm}^3$, $T = 100\,\text{eV}$ and $P = 640.3\,\text{bar}$, correspondingly. The ideal gas equation of state with $\gamma = 5/3$ was used for the target, and the pressure - temperature relation in the form $P = 2nkT$ accounted the ion and electron pressure of the fully ionized target material.

Simulation verified that the liner density increases proportionally to r^{-2} during the implosion, as predicted in [8] (see Figure 1). The liner density profile before the interaction with the target is shown in Figure 2. After the contact with the liner, the target was almost adiabatically compressed until it reached the stagnation point at time 6 μs. The fully compressed target radius was 0.73 cm, and the corresponding compression ratio was 6.8. By "almost adiabatic

compression" we mean that a small component of the stagnation pressure can be attributed to the shock wave sent by the liner: while the adiabatic compression would result in the stagnation pressure of 9.3 Mbar, the maximum pressure observed in the target was 11 Mbar. In simulations, the liner failed to compress the target to $R = 0.5$ cm, the expected compressed radius of the theoretical model. As the pressure during the adiabatic compression increases proportionally to the fifth power of the compression ratio, smaller target compression led to a much smaller stagnation pressure compared to theoretical model: [8] predicted 64 Mbar for to the compression ratio of ten. The resulting decrease of the fusion energy gain in simulations is analysed below.

The evolution of the liner - target interface near the stagnation point is shown in Figure 3. The velocity of the initial target expansion is approximately 0.58 $cm/\mu s$. Below we compare main quantities used in theoretical estimates such as the deconfinement time, the hydrodynamic efficiency, and the fuel burn-up fraction predicted by theory and simulations. Although these quantities are not explicitly used in simulations for obtaining the energy gain, their calculation from simulation data and comparison with theoretical predictions is useful for a better understanding of the theoretical model.

Deconfinement time. Figure 4 depicts the evolution of the normalized pressure in the target and the normalized fusion energy in the vicinity of the stagnation point. It shows that the fusion gain is more than 90% complete after the pressure in the target is reduced by the factor of two. This justifies the definition of the deconfinement time given above. The deconfinement time calculated from this pressure plot is equal to 220 ns, which is 2.2 times bigger than the estimate of [8]. Formula (9), applied to computed target - liner propetries at stagnation, gives the deconfinement time of 114 ns while the left hand side of formula (8) ($2R/u_j$) gives the value of 146 ns. Both theory and simulations results are significantly different from estimates obtained with a converging shock model [10] which are of the order of 1 μs.

Hydrodynamic efficiency. The hydrodynamic efficiency calculated using the simulation data and formula (6) gives the value of 0.016. The corresponding theoretical value reported in [8], obtained using (7), is 2.5 times larger: $\eta = 0.04$

Fuel burn-up fraction. The total number of fusion neutrons, obtained in simulations during the entire target evolution, divided by the total initial number of atoms in the target gives the value of the burn-up fraction as 6.67×10^{-4}. The corresponding theoretical prediction is 16.5 times bigger: [8] reports 0.011. The reason for such a big discrepancy is that, despite the longer deconfinement time, the temperature in the target remains well below 10 keV. Even at the maximum compression, only small central spot in the target reached the temperature higher than 10 keV while the volume averaged temperature $\overline{T} = \int_0^R T(r) r^2 dr / \int_0^R r^2 dr$ was only 5.2 keV.

Distributions of density, pressure, and temperature at the stagnation point are shown in Figures 5.

Fusion energy gain. The total fusion energy gain achieved in the simulation was 0.012. This value is 10.8 times smaller than the theoretical prediction. The value reported in [8] is 0.026 using the coefficient 0.2 as the electromagnetic efficiency of the plasma gun. Since we do not consider specific values of the electromagnetic efficiency in this work, the corresponding theoretical value is 0.13. Such a large discrepancy between the theory and simulation is due to the failure of the liner to compress the target to the radius of 0.5 cm and can be easily explained by the theoretical scaling law. Assuming that the fusion reactivity in the vicinity of the ignition temperature scales

as T^2, we can derive from (3) and (4) that the fusion gain scales as

$$G \sim P\,\tau_{dc}\,\eta_h. \tag{10}$$

Comparing the stagnation pressures, deconfinement times and hydrodynamic efficiencies of the theoretical model and simulation, we conclude that the scaling law predicts 6.5 times smaller fusion gain for the compressed target achieved in the simulation compared to theoretical prediction. Since the actual gain was 10.8 times lower, the discrepancy between the theory and simulation in the sense of the scaling law is approximately 1.7.

To complete the discussion, we also employed the idealized "solid target" model of [8] for the purpose of verification of theoretical predictions. In this model, the plasma target offers no resistance to the liner after the collision of the inner liner surface with the initial target surface. The target freely compresses until it reaches the final compressed state R and then suddenly responds to the liner with infinite resistance. The target pressure sharply increases and reaches the stagnation pressure $P_{\rm st}$. In the computer code, this process was modeled by inserting a solid ball in the center of the chamber with the radius equal to the compressed target radius of $R = 0.5$ cm. The solid target model was used to compute the dependence of the logarithm of the ram pressure amplification factor A vs. the logarithm of the compressibility factor $C = r_m/R$. Results are summarized in Figure 6. We define the ram pressure amplification factor as

$$A = \frac{P_{\rm st}}{\rho_m * V_m^2},$$

where ρ_m and V_m are the initial density and velocity of the liner (or density and velocity of plasma jets at the merging radius). In agreement with theoretical predictions, plots of the simulation data never exceed the ideal line $A = C^2$ (line 1 in Figure 6). According to the theory, A initially increases as C increases and then diverges from the ideal line towards saturation (constant A) regime. Such a behavior was obtained for the $M = 60$ liner with adiabatic index $\gamma = 5/3$ (curve 3). Simulations at Mach number 60 and $\gamma = 1.3$ have not reached the saturation at realistic values of the compressibility factor (curve 2). In numerical simulations with low Mach number liners (M = 20), A reached its maximum value at some radial compression value ($\log_{10} C \simeq 2.15$), and then slightly decreased. In agreement with the theory, the point of divergence from the monotonic increase of A can be increased by increasing of the Mach number or reducing of the adiabatic index γ.

1.4 Scaling laws and the fusion gain improvement

In this section, we investigate a possibility of improving the fusion energy gain by varying target and liner parameters within reasonable limits. Theoretical predictions of the impact of parameters on the fusion gain is summarized in the scaling law derived from Parks formulas [8]:

$$G = 10^{-4} \frac{< \sigma v >_{DT}}{T^{3/2}} \frac{R^2}{L_{\rm jet}} (n_0 n_L)^{1/2} \left(\frac{m_{\rm jet}}{2.5}\right)^{1/2} C_L C_T^{3/2} \frac{\eta_E}{0.25} \tag{11}$$

$$= 10^{-4} \frac{< \sigma v >_{DT}}{T^{3/2}} \frac{r_m\, R_0}{\sqrt{R} L_{\rm jet}} (n_0 n_L)^{1/2} \left(\frac{m_{\rm jet}}{2.5}\right)^{1/2} \frac{\eta_E}{0.25}$$

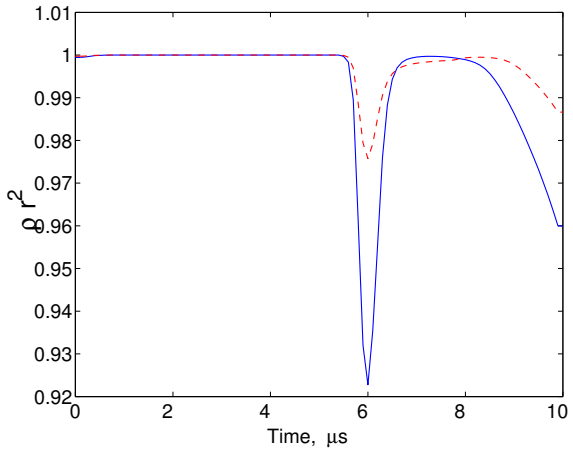

Figure 1: (Color online) Verification of the density scaling $\rho \sim 1/r^2$. Solid line: maximum density in the liner; dashed line: average density across the liner.

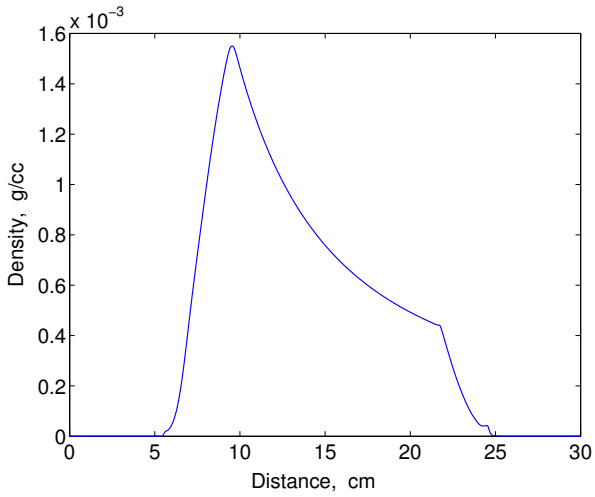

Figure 2: (Color online) Density profile of the DT liner before the interaction with the target.

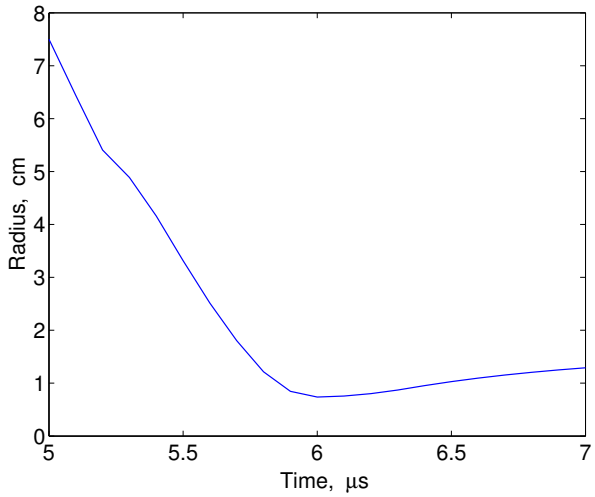

Figure 3: (Color online) Evolution of the liner - target interface near the stagnation point for DT liner with initial thickness of 15 cm.

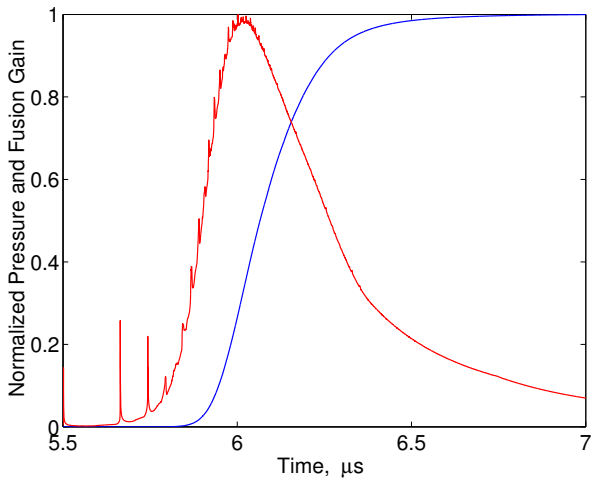

Figure 4: (Color online) Evolution of normalized pressure and normalized fusion energy during target deconfinement for DT liner with initial thickness of 15 cm.

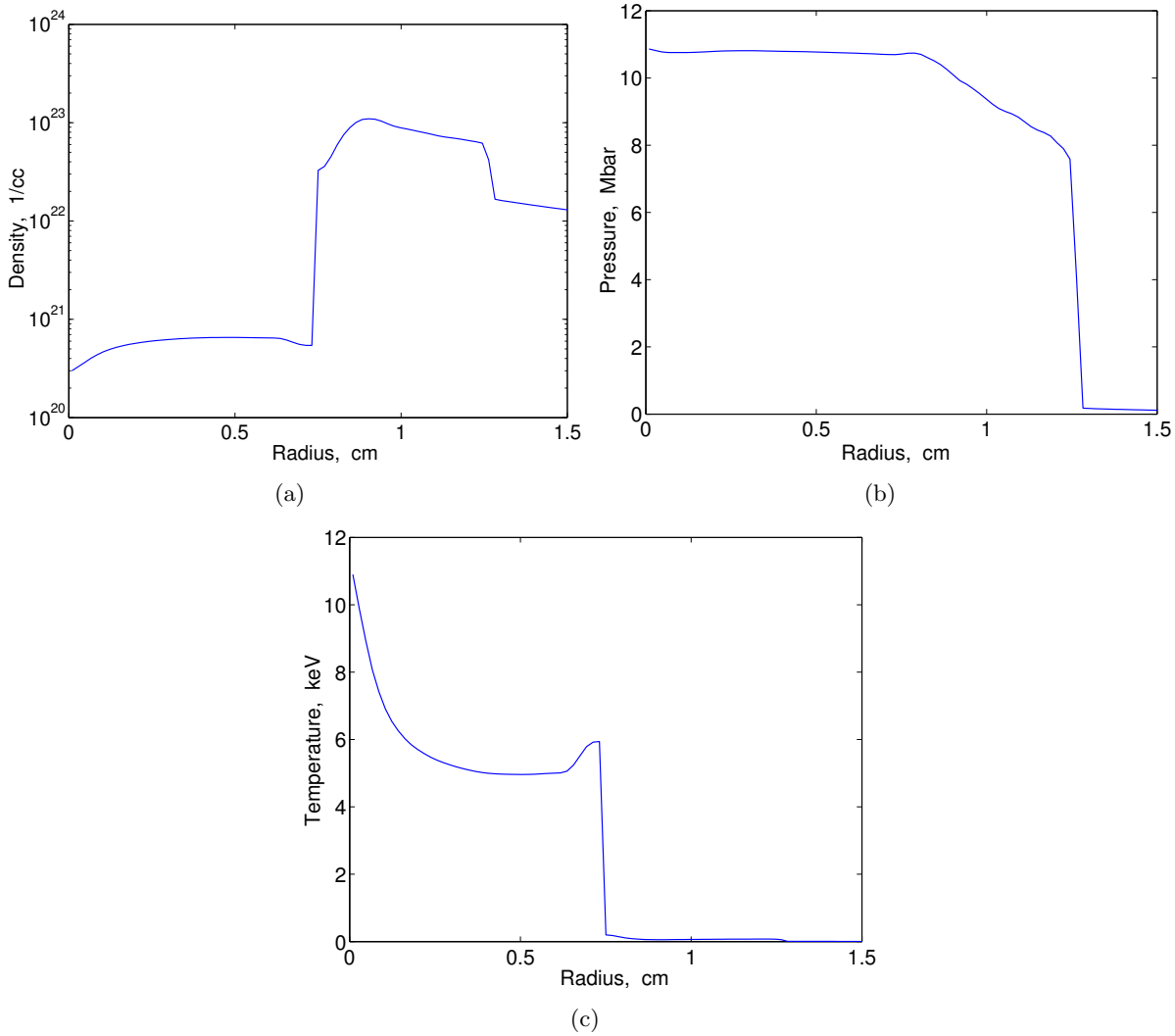

(a) (b) (c)

Figure 5: (Color online) Density, pressure and temperature at maximum target compression for DT liner with initial thickness of 15 cm.

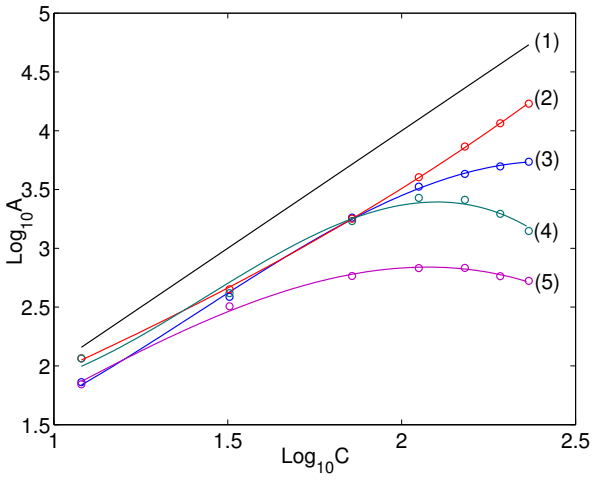

Figure 6: (Color online) Logarithm of the ram pressure amplification factor A vs. logarithm of the radial compression C. Plot (1) corresponds to the ideal model $A = C^2$. Other plots obtained using simulation data. (2): Mach number 60 and adiabatic index $\gamma = 1.3$, (3): Mach number 60 and $\gamma = 5/3$, (4): Mach number 20 and $\gamma = 1.3$, and (5): Mach number 20 and $\gamma = 5/3$. Circles represent numerical simulation data points and solid lines represent the least squares fit of numerical data by cubic polynomials.

where T and R are the target temperature and radius at stagnation (cm), n_0 is the initial target density (cm^{-3}), $L_{\rm jet}$ is the length of jets forming the liner (cm), n_L is the initial liner density (cm^{-3}), $m_{\rm jet}$ is the jet ion mass (amu), $C_L = R_m/R$ is the radial convergence of the liner, $C_T = R_0/R$ is the radial convergence of the target, and η_E is the electric gun efficiency which is equal to one throughout this paper.

As (11) suggests, the fusion energy gain increases with the reduction of the liner thickness provided that such a liner is still capable of compressing the target. A thin liner carries less initial kinetic energy and increases the fusion energy gain by higher values of the hydrodynamic efficiency. We performed simulation reducing the liner thickness to 5 cm and leaving other parameters of the previous setup unchanged. Numerical results showed that the 5 cm deuterium liner has the same ability to compress the target to the fusion condition: the compressed target radius as well as profiles of the temperature, density and pressure at stagnation, and the evolution of pressure (deconfinement time) are practically identical to those for the 15 cm liner. A small difference in details of the thermodynamic profiles at stagnation contributes to 1.9% decrease of the total fusion energy of the target compressed by the 5 cm liner. In agreement with the scaling law, the fusion gain increases by 3.4 times compared to the 15 cm liner. Notice that the increase of the length of plasma jets forming the liner is not identical to the increase of the liner thickness in a 1D model and the 15 cm thick liner carries 3.5 times larger kinetic energy compared to 5 cm thick liner. Further reduction of the liner thickness for the purpose of the fusion gain increase is not practical as the propagation of very short plasma jets prior to their merger will result in the spreading of their density.

In the previous section, we assumed that alpha particles produced in the nuclear fusion

process escape the target without interaction with the target material. Here we employ a very simplified model for the absorption of alpha particles in order to evaluate its effect on the target temperature, pressure, and the fusion energy gain. We assume that some fraction of alpha particles are absorbed locally and deposit their energy of 3.5 MeV per alpha particle. Numerically, we added the energy of the alpha particles to the same computational cells where particles were created. We used 0.35 as the alpha particle absorption coefficient in most of simulations. Anticipating larger burn-up fractions of targets, we also reduced the density of the target at each time step proportionally to the reaction products that left the target.

The inclusion of alpha particle heating had very small effect on the stagnation state and fusion gain of the target compressed by the 15 cm thick deuterium-tritium liner. While the stagnation state was practically identical in both cases, the alpha heating resulted in slightly higher values of the pressure and temperature during the deconfinement process and contributed to the fusion gain increase of 4.3%. As we will see later, the alpha particle heating has much bigger effect on large targets compressed by heavy xenon liners.

In the next simulation series, we replaced the deuterium liner with a 5 cm thick xenon liner with density $\rho = 8.5 \times 10^{-4}\,\mathrm{g/cm^3} \simeq 4 \times 10^{18}\,1/\mathrm{cm^3}$, temperature $T = 2.27\,\mathrm{eV}$, pressure $P = 14.2\,\mathrm{bar}$, velocity $v = 100\,\mathrm{km/s}$, and Mach number $M = 60$. The total kinetic energy of such a liner is 1 GJ. We also increased the initial target radius to 10 cm. The heavy liner compressed the target to R = 0.84, slightly exceeding the compression ratio of 10. The pressure reached 265 Mbar but some transient pressure peaks associated with the focusing of shock waves during the target compression reached 287 Mbar. The volume averaged temperature was 32.6 keV while the temperature in the target center reached 65 keV. The alpha heating caused slight increase of the averaged temperature during early stages of the target expansion. The highest averaged temperature of 36.8 was reached at $6.3\,\mu s$ or 300 ns after stagnation. Since the deconfinement time was 200 ns, the highest temperature was reached at $1.5\tau_{dc}$. The computed value of the deconfinement time agrees reasonably well with the theory: $2R/u_j = 168$ ns while formula (9) gives 141 ns. The inclusion of alpha heating and the resulting increase of temperature after stagnation does not require modifications of the definition of deconfinement time: the nuclear fusion process was completed by 84% when the pressure dropped by half. The fusion gain obtained in simulations was 2.6 or 217 times bigger compared to the 15 cm deuterium liner setup. The scaling law (11) predicts the fusion gain of 12.8.

Keeping the liner unchanged, we performed a series of simulations by increasing the target radius to 30 cm with 5 cm increments. The dynamics of the corresponding fusion gains is plotted in Figure 7. We observed that the 20 cm target was the most optimal for the given liner: it achieved the compression ratio of 10, the stagnation pressure of 130 Mbar (the pressure increase is higher than predicted by the adiabatic compression law because of the alpha heating), the average temperature of 16 keV, and produced the fusion gain of 10. Alpha heating caused futher increase of the target temperature during deconfinement and the average temperature reached the maximum value of 23.3 keV at 200 ns after the stagnation. The computed value of the deconfinement time was 150 ns and theoretical predictions are as follows: $2R/u_j = 400$ ns while formula (9) gives 360 ns. The profiles of density, pressure, and temperature at stagnation and 200 ns after stagnation are shown in Figure 8. The value of the fusion gain calculated from the scaling law (11) is 30. The interplay between the target size, compression ratio, and the stagnation temperature led to smaller values of the fusion gain for smaller and bigger targets:

$G = 6.7$ for 15 cm radius target, $G = 7.0$ for 25 cm target, and $G = 2.5$ for 30 cm radius target in the presence of alpha heating. While the small target size was the critical factor for 10 and 15 cm targets, smaller stagnation temperatures for 25 and 30 cm targets contributed to reduced fusion gains.

In order to evaluate the effect of alpha heating for targets producing significant egergy gains, we performed the same series of simulations with the alpha heating turned off. Results are illustrated in Figure 9. The absence of alpha heating reduced the fusion gain of 15 cm target to 5.6 while the fusion gain for 20 cm target was reduced to 6.0. The corresponding theoretical value for the 20 cm target obtained from (11) is 27.6. Therefore the scaling law predicts approximately 4 times higher fusion gain compared to simulations because higher target compression rates are assumed in theoretical estimates.

It was suggested in the original paper on the plasma jet MIF [9] that the inner layer of a composite liner containing deuterium-tritium inner part and an outer xenon pusher may provide additional fuel for the thermonuclear reaction. For testing of this idea, we included a 5 cm deuterium layer in front of a 5 cm xenon layer. The initial density was $3.8 \times 10^{-5}\,\mathrm{g/cm^3}$ for the deuterium layer, $8.5 \times 10^{-4}\,\mathrm{g/cm^3}$ for the xenon layer, the initial pressure was 14.2 bar in both layers, and the Mach number was 60 in xenon and 12.5 in deuterium, correspondingly. The liner was used to compress the 20 cm radius target that gave the highest fusion gain for the single-layer xenon liner. Because of high pressure and much lower Mach number in the deuterium layer compared to the single deuterium liner simulations, the deuterium layer quickly spread out reaching the thickness of 10 cm before the interaction with the target. Then the process consisted in the compression of both the deuterium layer and the target. At stagnation, the deuterium liner thickness was only 6 mm while the target was compressed to 2.4 cm. Because of the compression of the deuterium liner layer, the pressure in the target reached only 57 Mbar while the average temperature in the target was about 14.5 keV. Without α-heating of the liner layer, the released fusion energy was reduced by 2 times compared to the single xenon liner case. The compression of the deuterium layer of the liner raised the temperature in the liner at the target - liner interface to 4.5 keV at stagnation and the temperature was reduced to 1 keV within 2 mm. Therefore the fusion energy production in the deuterium layer was negligible without the α-heating. The state of the target at stagnation is shown in Figure 11. The use of the composite deuterium - xenon liner also reduced the fusion production of the 10 cm target by 2 times and 30 cm target by 1.5 times. In a forthcoming paper, the effect of alpha heating of the inner liner layer will be addressed.

1.5 Conclusions

Using the method of front tracking, we have performed spherically symmetric simulations of the implosion of plasma liners and compression of targets related to the plasma jet driven magneto inertial fusion. The study of the ram pressure amplification factor A and its dependence on the radial compressibility $C = r_m/R$ is in good agreement with theoretical predictions. Simulations of a deuterium-tritium target with the initial radius $r = 5$ cm, density $n = 2 \times 10^{18}\,1/\mathrm{cm^3}$, and temperature 100 eV, compressed by a 15 cm thick deuterium liner with the initial radius of 60 cm, density of $9.2 \times 10^{18}\,1/\mathrm{cm^3}$ and Mach number 60, have been compared in details with theoretical predictions of [8]. Simulations showed that such a liner will not be able to achieve

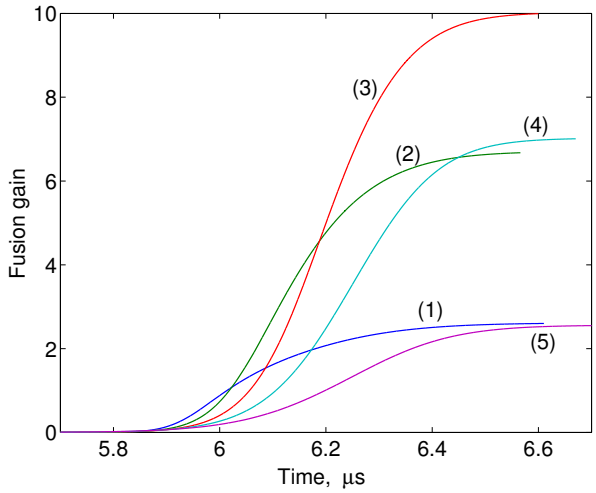

Figure 7: (Color online) Dynamics of the fusion gain of targets compressed by 5 cm thick single layer xenon liner. Initial target radii are: 10 cm (1), 15 cm (2), 20 cm (3), 25 cm (4), and 30 cm (5).

the compression rate of 10 obtained in the theoretical work. In simulations, the target was compressed to $R = 0.73$ cm at stagnation. It reached the pressure of 11 Mbar and produced 10.8 smaller amount of the fusion energy compared to the theory. However when the theoretical scaling law was used to estimate the fusion gain of the target compressed by 6.8 times to the stagnation radius of 0.73 cm, the disagreement with the theory was only by the factor of 1.7. Simulations showed that the inclusion of alpha particle heating had very small effect on the fusion gain in this liner - target setup: the local deposition of the energy of alpha particles using the absorption coefficient of 0.35 increased the fusion gain by only 4.3%. In agreement with the scaling law, the fusion energy gain increased with the reduction of the initial liner thickness to 5 cm since such a liner, while carrying 3.5 times smaller kinetic energy, has the same ability to compress the target as a much thicker one: the profiles of pressure, density and temperature at stagnation and the deconfinement time are practically identical to ones obtained with 15 cm thick liner. Further reduction of the liner thickness seems impractical because of the diffusion of short plasma jets during their propagation from the plasma gun to the merging point.

We have also investigated the fusion gain produced by larger targets compressed by heavy xenon liners and double layer deuterium - xenon liners. With the inclusion of alpha heating, the fusion energy gains significantly improved and reached 10 in the most optimal setup for a given chamber size: 20 cm radius target compressed by a single layer xenon liner. The theoretical formula for the fusion gain predicts approximately 4 times higher fusion gain compared to simulations because the theoretical target compression rates are higher. For all simulations, deconfinement times calculated from simulation data agreed within the factor of two with theoretical formulas of [8] and were significanly lower compared to estimates of the order of 1 μs obtained with the converging shock model of [10].

Turning off the alpha particle heating reduced the fusion gain by 1.7 times. The double layer deuterium - xenon liners, expected to provide extra fuel for the thermonuclear reaction, have

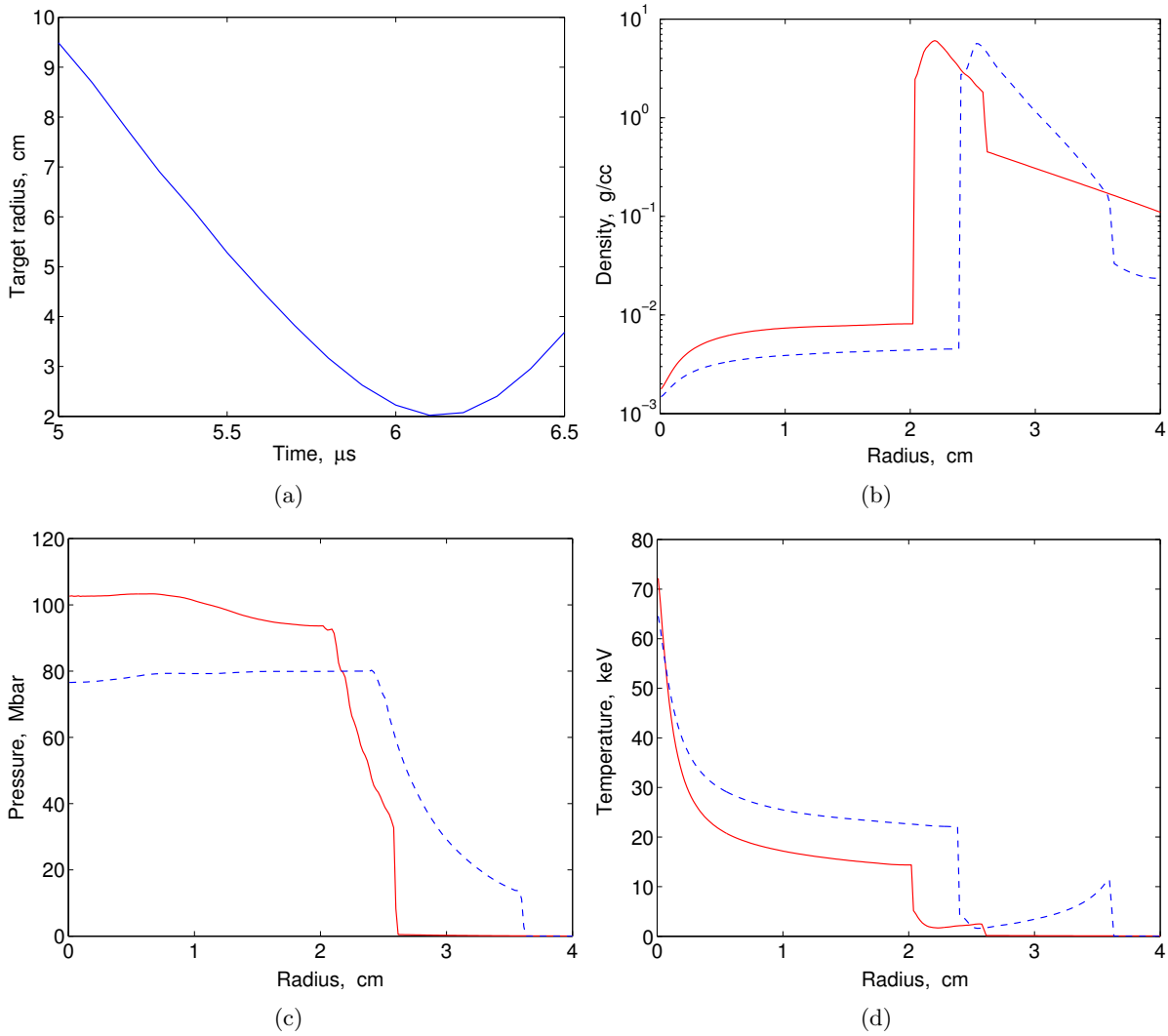

Figure 8: (Color online) Target surface evolution (a) and density (b), pressure (c), and temperature (d) at stagnation (solid line) and 200 ns after stagnation (dashed line) of initially 20 cm target compressed by the 5 cm thick xenon liner.

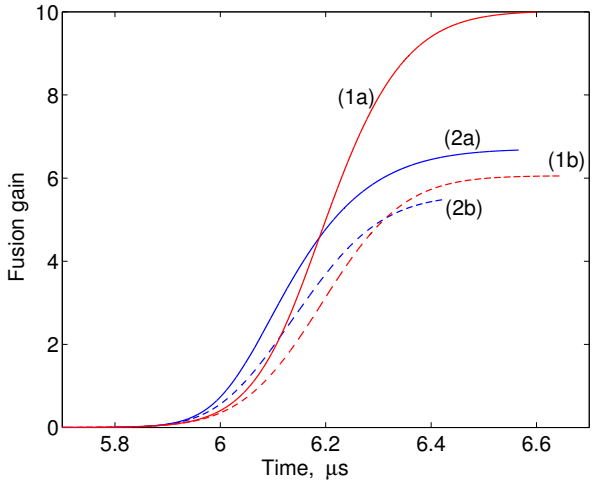

Figure 9: (Color online) Influence of alpha heating on the fusion gain of targets compressed by 5 cm thick single layer xenon liner. Solid lines show the fusion gain in the presence of alpha heating and dashed lines show the fusion gain when alpha heating was turned off. Initial target radii are: 20 cm (1a,b) and 15 cm (2a,b).

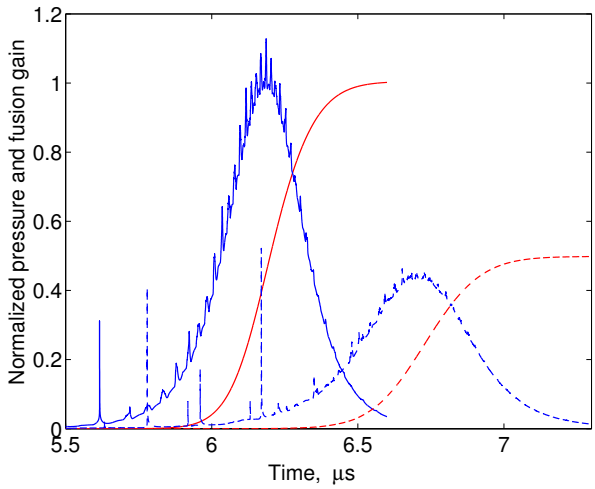

Figure 10: (Color online) Normalized pressure and fusion gain of the 20 cm target compressed by the single 5 cm thick xenon liner (solid line) and the composite liner containing 5 cm thick interior deuterium-tritium layer and 5 cm thick outer xenon layer.

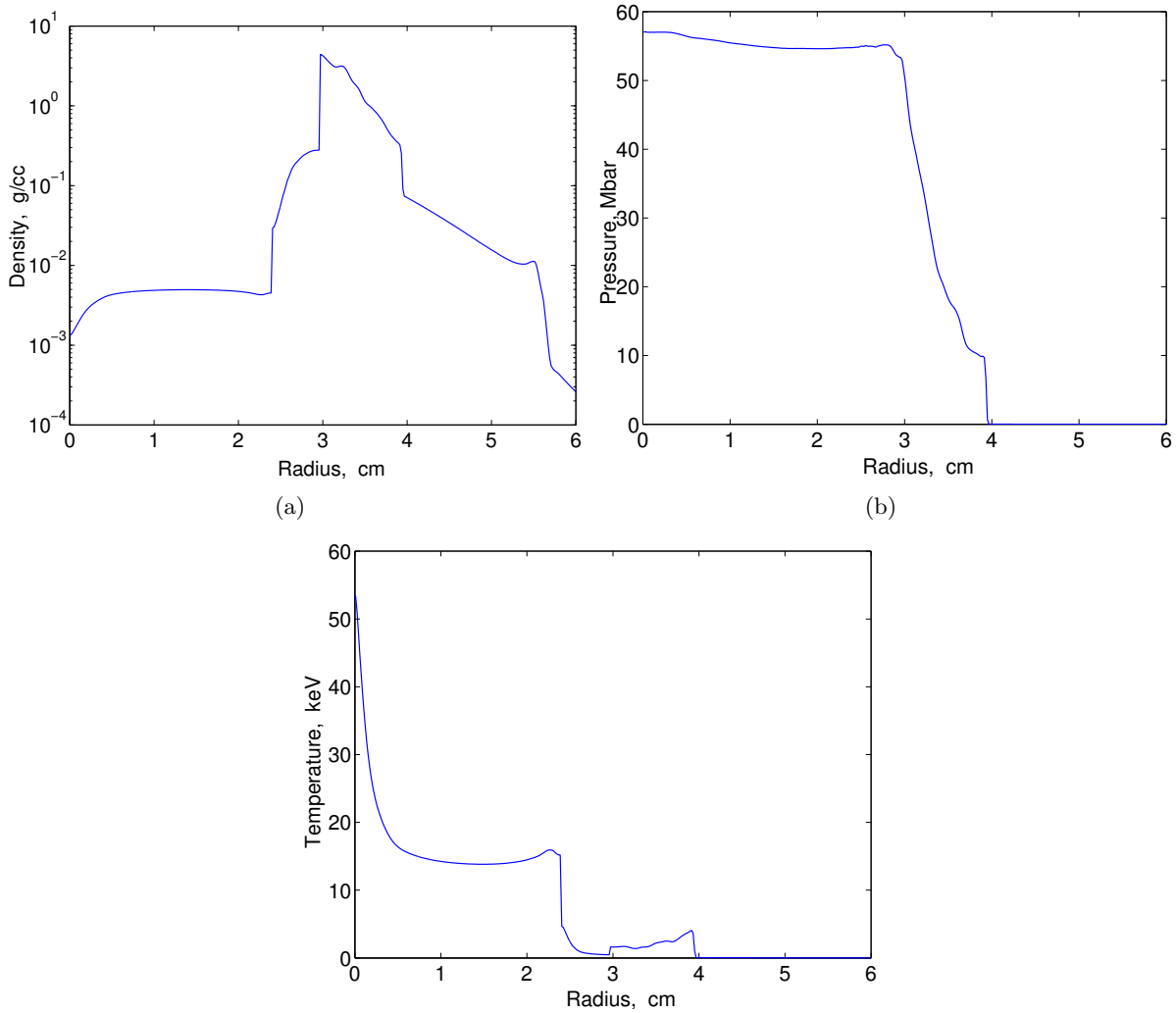

Figure 11: (Color online) Density (a), pressure (b), and temperature (c) at stagnation (solid line) and 200 ns after stagnation (dashed line) of initially 20 cm target compressed by the composite deuterium - xenon liner.

been simulated as well. Because of the compression of the deuterium liner layer, the compression ratio of the target decreased. Without the α-heating of the inner liner layer, the fusion gain was twice smaller for the 20 cm target. Similar reductions were observed for different target sizes. Simulations showed that the compression of the inner liner layer is not sufficient to achieve the ignition without α-heating. This effect will be investigated in the future work.

A forthcoming paper will use the front tracking method for full 3D simulations of the propagation and merger of plasma jets, and the formation and implosion of liners with resolving oblique waves and hydrodynamic instabilities.

2 Influence of Atomic Processes on the Implosion of Spherically-symmetric Plasma Liners

2.1 Summary

The influence of atomic physics processes on the implosion of plasma liners for magneto-inertial nuclear fusion has been investigated numerically by using the method of front tracking in spherically symmetric geometry and equation of state models accounting for dissociation and ionization. Simulation studies of the self-collapse of argon liners to be used in the Los Alamos Plasma Liner Experiment (PLX) program have been performed as well as studies of implosion of deuterium and argon liners on plasma targets . Results show that atomic processes in converging liners reduce the temperature of liners and increase the Mach number that results in the increase of the stagnation pressure and the fusion energy gain. For deuterium and argon liners imploding on plasma targets, dissociation and ionization increased the stagnation pressure and the fusion energy gain by the factor of 1.5 (deuterium) and 2 (argon) correspondingly. Similarly, ionization during the self-collapse of argon liners lead to approximately doubling of the Mach number and the stagnation pressure. The influence of the longitudinal density spread of the liner has also been investigated. The self-collapse stagnation pressure decreased by the factor of 8.7 when the initial position of the liner was shifted from the merging radius (33 cm) to the PLX chamber edge (137.2 cm). Simulations with and without the heat conduction demonstrated that the heat conduction has negligible effect on the self-collapse pressure of argon liners. This Section is based on [2].

2.2 EOS with atomic processes

The processes of dissociation (of diatomic gases) and ionization of atoms introduce significant energy sinks and strongly affect the plasma temperature and the Mach number. In the next two sections, we briefly describe EOS models with atomic processes for the deuterium molecular gas and high-Z monatomic gases and their implementation in the FronTier code.

2.2.1 EOS for deuterium

A deuterium EOS model and its implementation was described in detail in [11]. For completeness, we repeat here the main formulas. The pressure and specific internal energy of a partially

dissociated and partially ionized diatomic gas can be written as

$$P = \left(\frac{1}{2} + \frac{1}{2}f_d + f_i\right)\frac{\rho kT}{m_a} \tag{12}$$

$$E = \left(\frac{1-f_d}{2(\gamma_m - 1)} + \frac{f_d + f_i}{\gamma - 1}\right)\frac{kT}{m_a} + \frac{1}{2}f_d\frac{k\epsilon_d}{m_a} + f_i\frac{k\epsilon_i}{m_a}, \tag{13}$$

where γ_m and $\gamma = 5/3$ are specific heat ratios for molecules and atoms, respectively, k is the Boltzmann constant, m_a is the mass of the atom(ion). The dissociation $f_d(\rho, T)$ and ionization $f_i(\rho, T)$ fractions are defined as

$$f_d = (n_a + n_i)/n,$$
$$f_i = n_i/n,$$

in which $n \equiv 2n_g + n_a + n_i = \rho/m_a$ stands for the total number density of *nuclei*, and n_g, n_a, and n_i denote, respectively, the number densities of gas D_2 molecules, D atoms, and D^+ ions. For deuterium, the dissociation energy is $\epsilon_d = 4.48$ eV, and the ionization energy is $\epsilon_i = 13.6$ eV. The dissociation and ionization fractions can be found from Saha equations [12]. For deuterium, they can be written (in eV units) as

$$\frac{f_i^2}{1-f_i} = 3.0 \times 10^{21}\frac{T^{\alpha_i}}{n}\exp\left(-\frac{\epsilon_i}{T}\right), \tag{14}$$

$$\frac{f_d^2}{1-f_d} = 1.55 \times 10^{24}\frac{T^{\alpha_d}}{n}\exp\left(-\frac{\epsilon_d}{T}\right), \tag{15}$$

where $\alpha_i = 3/2$ and the parameter α_d is chosen to be 0.327 for the best approximation of deuterium thermodynamic data [13]. To find pressure as a function of density and specific internal energy, as required by hydrodynamic code solvers based on primitive variables, we solve the quadratic equations (14) - (15) for f_i and f_d respectively. Substituting these solutions into the energy equation (13), a nonlinear equation $\Phi(\rho, E, T) = 0$ is obtained which can be solved for T for given values of ρ and E. Then this temperature value is used to calculate the dissociation and ionization fractions and the pressure. However, most of advanced numerical discretization algorithms, including second order MUSCL type schemes and interface propagation algorithms implemented in the FronTier code [5], use characteristic variables and solutions of Riemann problems across cell boundaries. Solving numerically a Riemann problem requires an ability to calculate the sound speed and integrals of Riemann invariant type expressions along characteristics. For this purpose, explicit expressions for the entropy, sound speed, and other thermodynamic properties of the system (12) - (15) were derived in [11] based on the second law of thermodynamics. To speed-up the calculation of Riemann-type invariants, precomputed tabulated data sets are often used.

2.2.2 EOS for high-Z materials

Suppose a high-Z monatomic gas can achieve multiply ionized states with the ionization energies $I_1, I_2, \ldots, I_Z$. The pressure and specific internal energy can be written as

$$P = (1 + f_e)\frac{\rho kT}{m_a} \tag{16}$$

$$E = \frac{3}{2}(1+f_e)\frac{kT}{m_a} + \frac{1}{m_a}\sum Q_m f_m + \frac{1}{m_a}\sum W_m f_m, \tag{17}$$

where f_e and f_m are fractions of electrons and ions with the ionization degree m, $Q_m = I_1 + I_2 + \ldots + I_m$ is the energy required to remove m electrons, I_m is m-th ionization potential, and W_m is the electronic excitation function. The fractions f_e and f_m satisfy the following conservation laws

$$\sum_m f_m = 1, \quad \sum_m m f_m = f_e,$$

and in the assumption of local thermodynamic equilibrium are governed by the system of Saha equations

$$\frac{f_{m+1} f_e}{f_m} = \frac{2m}{\rho}\frac{u_{m+1}}{u_m}\left(\frac{2\pi m_e kT}{h^2}\right)^{3/2}\exp\left(-\frac{I_{m+1}}{kT}\right), \quad m = 1, \ldots, Z, \tag{18}$$

where h is the Planck constant and u_m, $m = 1, \ldots, Z$ are known electron partition functions. Since the system of Saha equations (18) is a coupled system of Z nonlinear equations, solving them in an EOS library of a hydro code is prohibitively expensive. By introducing the continuum approximation of the ionization fractions, particle number densities, and the ionization energy function as in [12],

$$f_m \to f(m), \quad n_m \to n(m), \quad I_m \to I(m),$$

and satisfying the integral form of conservation laws

$$\int n(m)dm = n,$$

$$\int m\, n(m)dm = n_e,$$

the coupled system of Saha equations is reduced to a single ordinary differential equation

$$\left(1 + \frac{d\log n}{dm}\right) n_e = AT^{3/2}\exp -\frac{I(m+1)}{kT}. \tag{19}$$

The continuum representation of the argon ionization energies, shown in Figure 12, was obtained using a third order piece-wise polynomial approximation and the discrete energy spectrum of the argon atom.

The distribution of ionized states $n(m)$ at given density and temperature values resembles a sharp, Gaussian-type curve centered at the average ionization $\bar{m}$ defined as

$$\bar{m} = \frac{\int m\, n(m)dm}{\int n(m)dm} = \frac{n_e}{n} = m|_{\frac{dn}{dm}=0}\,.$$

From (19), the average ionization value is

$$\bar{m} = \frac{AT^{3/2}}{n}\exp -\frac{\bar{I}}{kT}. \tag{20}$$

The corresponding internal energy and pressure for average ionization modeling are

$$P = n(1+\bar{m})kT \tag{21}$$

$$E = \frac{3}{2}(1+\bar{m})\frac{kT}{m_a} + \frac{1}{m_a}Q(\bar{m}), \tag{22}$$

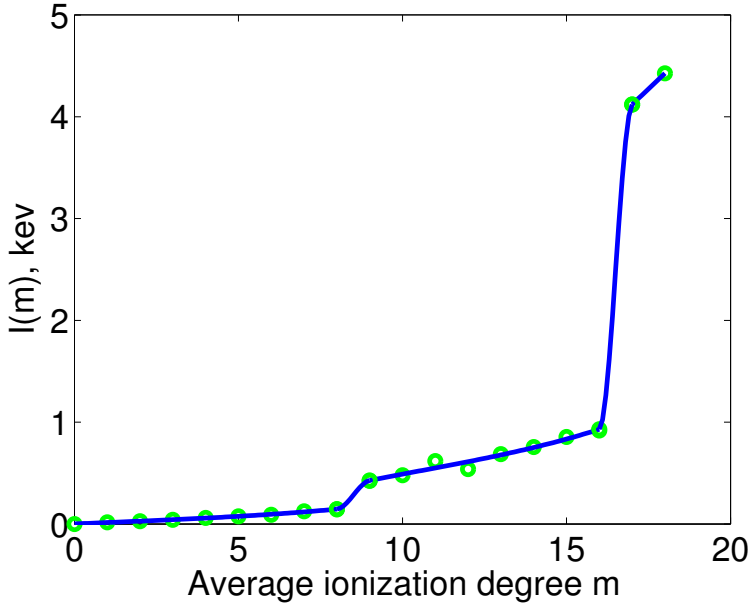

Figure 12: (Color online) Ionization energies of argon atom (circles) and their continuum representation by function $I(m)$ (solid line).

Following [12], we use the average ionization value for the calculation of thermodynamic quantities. Substituting (21) or (22) into the Saha equation(20) with the discrete functions I_m and Q_m replaced by the corresponding continuum functions describing specific material, we obtain a single nonlinear equation for finding $\bar{m}$ at given values of specific internal energy or pressure with value of density. Using the expression for entropy from [12] and the local gamma-law fit for other thermodynamic properties, we calculate the sound speed and other quantities required by the Riemann solver.

We have validated the average ionization EOS model by comparing with numerical solutions of the coupled system of Saha equations. In Figure 13, we plot the dependence of the average ionization level of argon gas on temperature for three density values: $5 \times 10^{-7}\, g/cm^3$, $5 \times 10^{-5}\, g/cm^3$, and $5 \times 10^{-3}\, g/cm^3$. Small discrepancies of ionization values near non-smooth sections of the curve have negligibly small effect on hydrodynamic states. The corresponding pressure curves obtained using the average ionization EOS model and the coupled system of discrete Saha equations are depicted in Figure 14 for the same values of density.

2.3 Simulation Results

2.3.1 Implosion of argon liners

This section reports simulation results of the self-implosion of argon liners and their implosion on solid targets. In [14], a number of 1d Lagrangian simulations of the implosion of argon liners with initial conditions relevant to PLX were performed. Simulations included the radiation

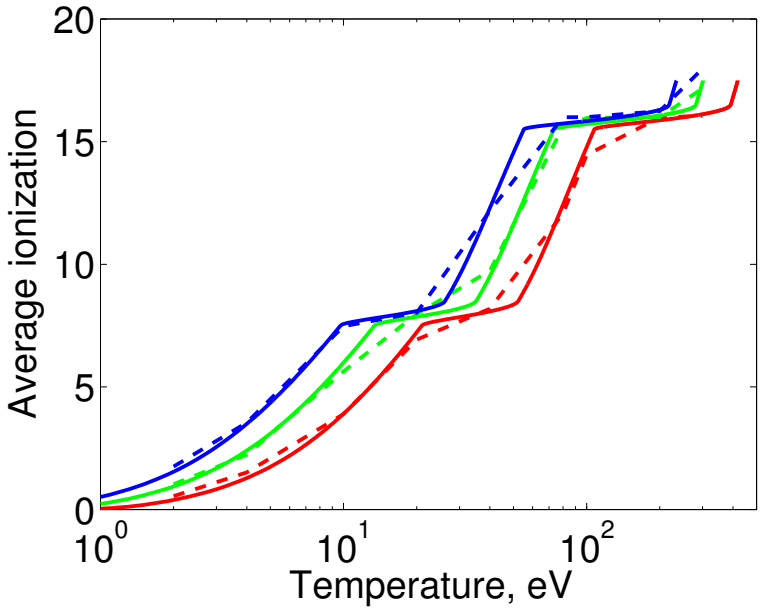

Figure 13: (Color online) Comparison of the average ionization calculated using the Zeldovich model (solid lines) and the full system of coupled Saha equations (dashed lines) at given temperature and three density values, $5 \times 10^{-3}\, g/cm^3$ (red bottom lines), $5 \times 10^{-5}\, g/cm^3$ (green middle lines), and $5 \times 10^{-7}\, g/cm^3$, (blue top lines) is shown.

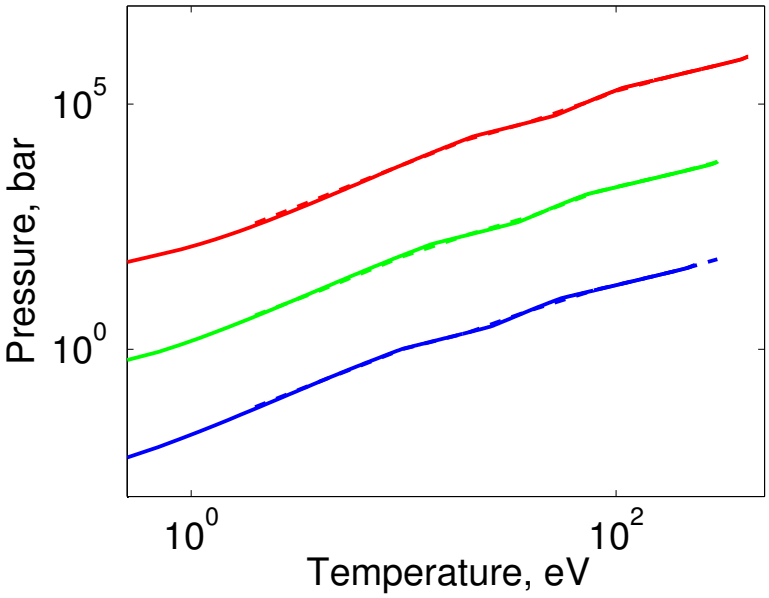

Figure 14: (Color online) Comparison of pressure values calculated using the Zeldovich model (solid lines) and the full system of coupled Saha equations (dashed lines). Temperature dependence of the argon gas pressure at three density values, $5\times10^{-3}\ g/cm^3$ (top lines), $5\times10^{-5}\ g/cm^3$ (middle lines), and $5\times10^{-7}\ g/cm^3$, (bottom lines) is shown.

transport which changes properties of the liner and can also suppress high temperatures of the vacuum region in front of imploding liners. However ideal gas EOS was used in most simulations of [14].

Using identical parameters to PLX1 and PLX2 numerical setups of [14], we performed simulations of the self-implosion of liners using the plasma EOS and compared them with results obtained in [14]. By excluding both the radiation transport and the heat conduction, we showed the relative importance of only atomic processes in the liner. To compare code results in more extreme regime, we also performed simulations using case 6 of Table II in [14]. Then we added the heat conduction and evaluated the role of the combined effect. We also showed the simulation results of the implosion on solid targets and discussed corresponding characteristic times.

For completeness, we provide here the initial parameters of PLX 1 and PLX 2 setups from [14]. For the PLX 1 simulation, the merging radius of the argon liner is 33 cm and the liner thickness is 44.7 cm. The initial state of the PLX1 liner is uniform with the density $\rho = 6.63 \times 10^{-8}\,\mathrm{g/cm^3} = 1.0 \times 10^{15}\,\mathrm{cm^{-3}}$, temperature $T = 2.8\,\mathrm{eV} = 32480\,\mathrm{K}$, pressure $P = 0.004482\,\mathrm{bar}$, velocity $v = 50\,\mathrm{km/s}$, and Mach number $M = 14.9$. The initial states of the PLX2 liner are same except that the thickness of the liner is 63.6 cm. Additionally, the initial state of the liner described in case 6 of Table II in [14] is also uniform with the density $\rho = 6.63 \times 10^{-7}\,\mathrm{g/cm^3} = 1.0 \times 10^{16}\,1/\mathrm{cm^3}$, temperature $T = 1.0\,\mathrm{eV} = 11604\,\mathrm{K}$, pressure $P = 0.02911\,\mathrm{bar}$, velocity $v = 50\,\mathrm{km/s}$, and the Mach number $M = 22.571$. For this case, the merging radius is 24.1 cm and the liner thickness is 25.5 cm.

The average ionization level of the initial liner was approximately 2.25 as the initial temperature ($T = 2.8\,\mathrm{eV}$) of the liner is comparable with the first ionization energies of the argon atom. This initial ionization gradually and very slowly increased during the implosion process. A significant increase of the ionization level and the corresponding changes of temperature and pressure occurred only at the last stage of the implosion. The profile of the average ionization across the liner close to the moment of stagnation is shown in figure 15(a). In the chamber center, it reaches 7.2. The corresponding profiles of the density, pressure, and temperature in the liner are shown in figures 15(b) - 15(d). We observe a factor of 6.5 increase of the density in the chamber center, the doubling of the stagnation pressure, and the reduction of temperature by the factor of 2.3. In figure 16, profiles of the argon liner sound speed and Mach number are depicted. Comparing with the result using polytropic EOS model, the Mach number is approximately 1.5 times higher when the plasma EOS model is used.

The temporal evolution of the maximum pressure in the liner during the self-implosion and implosion on the solid target is depicted in Figure 17. The implosion on the solid target produced higher peak pressure compared to the self-implosion. We explain this result by the influence of imperfect vacuum, namely by the ambient residual gas that was carried in front of the liner and mitigated the liner impact. Such a residual gas has a smaller effect in the case of a solid target of 5 mm radius compared to the zero-radius singularity associated with the self-implosion. We would like to note that maximum pressures achieved in our simulations are almost three orders of magnitude lower compared to [14]. Such a big difference is explained by the influence of the radiation transport. In both cases (solid target and self-implosion), atomic processes contributed to the stagnation pressure increase by approximately the factor of two.

As it was shown in [1], the thickness of the plasma liner has little effect on the target compression and the target deconfinement time. The deconfinement time was defined in [1]

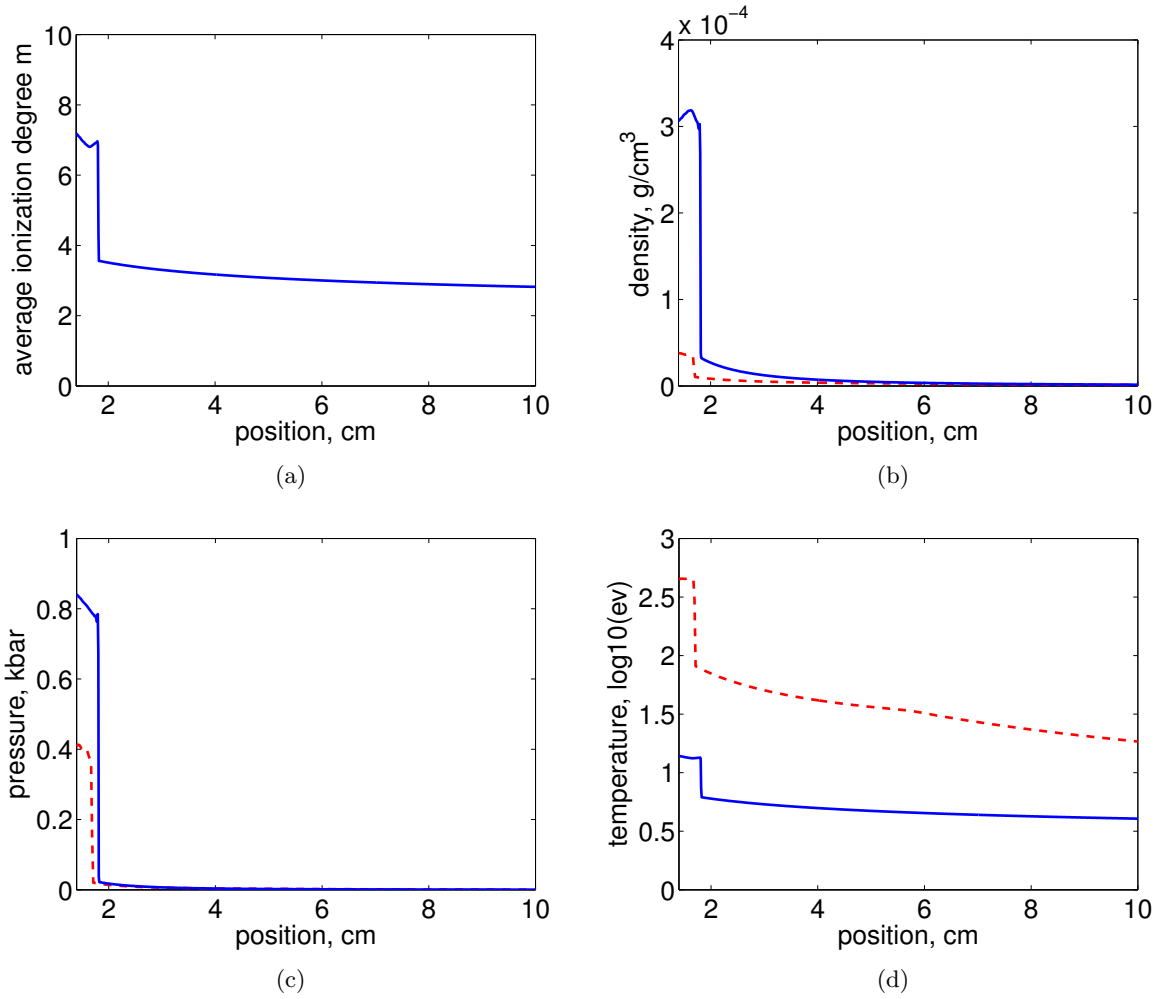

Figure 15: (Color online) average ionization (a), density (b), pressure (c), temperature (d) of the imploding argon liners around the stagnation time with PLX 1 parameters by using plasma EOS model (blue solid line) and polytropic EOS model (red dashed line).

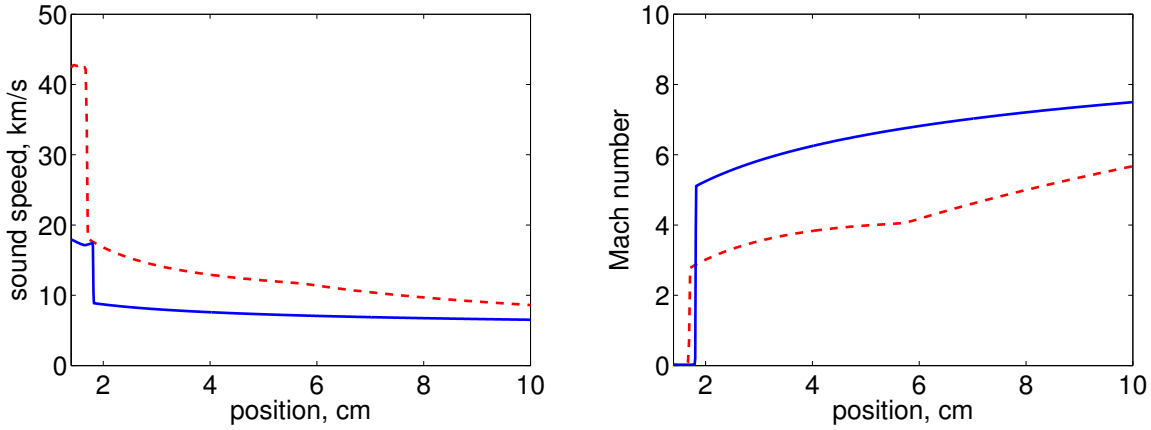

(a) (b)

Figure 16: (Color online) sound speed (a) and Mach number (b) of the imploding argon liners around the stagnation time with PLX 1 parameters by using plasma EOS model (blue solid line) and polytropic EOS model (red dashed line).

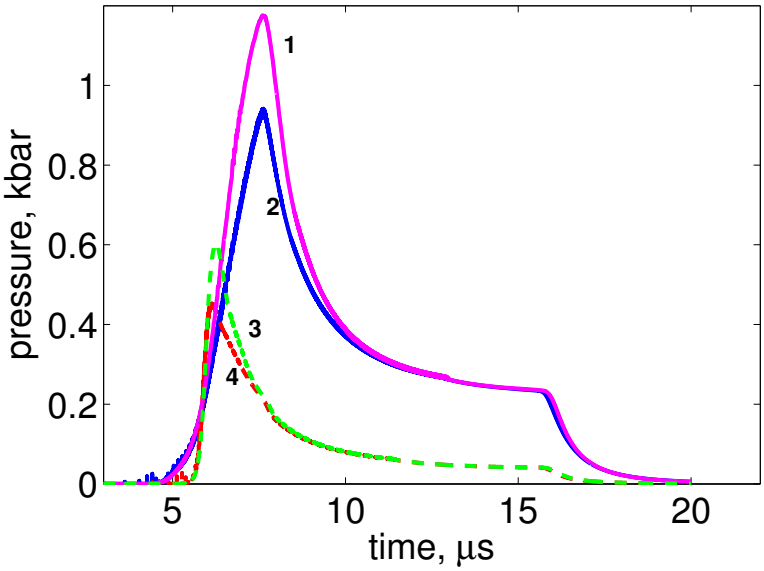

Figure 17: (Color online) Evolution of maximum pressure by using (1) plasma EOS with 0.5 cm solid target (purple solid line), (2) plasma EOS (blue solid line), (3) polytropic EOS with 0.5 cm solid target (green dashed line) and (4) polytropic EOS (red dashed line) of imploding argon liners with PLX 1 parameters. (Maximum pressure is picked among the values near liner's leading edge.)

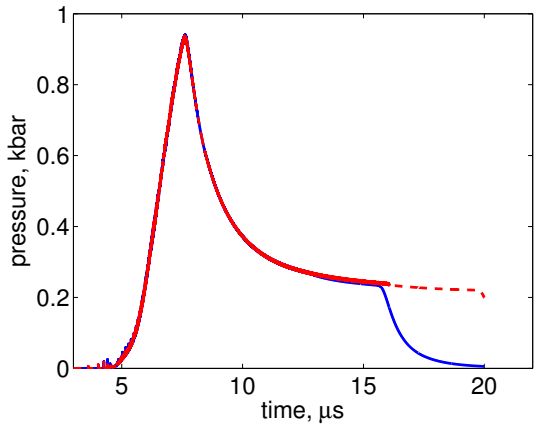

Figure 18: (Color online) Evolution of maximum pressure of PLX1 (blue solid line) and PLX2 (red dashed line).

as the time interval between the maximum compression time and the moment of time when the pressure falls by the factor of two. Such a definition was justified by the observation that nuclear fusion processes in the target were 95% completed when the pressure was reduced by the factor of two. The effect of thickness was verified in this work using argon liners. The evolution of the maximum pressure during the self-collapse of PLX1 and PLX2 liners, which differ only by their thickness, is shown in Figure 18. The pressure profiles and the deconfinement times in the sense of [1] are identical. As the described PLX experiment is designed to create conditions far below the fusion ignition, another characteristic time was used in [14] to describe the self-implosion process. It is defined as the time between the maximum compression peak and the time when the outgoing shock wave in the liner meets the rarefaction wave from the trailing edge of the liner causing an abrupt decrease of pressure. In the sense of this definition, the stagnation time increases with the increase of the liner thickness and is much larger than the value of deconfinement time according to the previous definition. While the stagnation time characterizes the existence of high energy density region produced by the self-collapse of the liner, the definition of the deconfinement time is more relevant when plasma liners are considered for the purpose of nuclear fusion. As the ionization influences mostly the narrow leading edge of the liner, the stagnation time was unaffected by the use of the plasma EOS.

In Figure 19, we provide simulation results related parameters of case 6 of Table II in [14] and compare them with Figures 5 and 12 in [14]. In the simulation using the polytropic EOS, the maximum pressure obtained by the FronTier code is placed between the values from the RAVEN and HELIOS codes in [14]. For the plasma EOS case, FronTier result obtained with the LTE plasma EOS is similar to the HELIOS code result obtained with PROPACEOS non-LTE EOS in [14]. The applicability of the local thermodynamic equilibrium assumption to the simulation of deuterium plasma liners is quantitatively analysed in the next section for deuterium liners. This analysis allow us to conclude that the LTE assumption is also valid for argon liners as the electron density only increases in the case of argon.

Initialization of the sharp liner profile at the merging radius of 33 cm was done for the

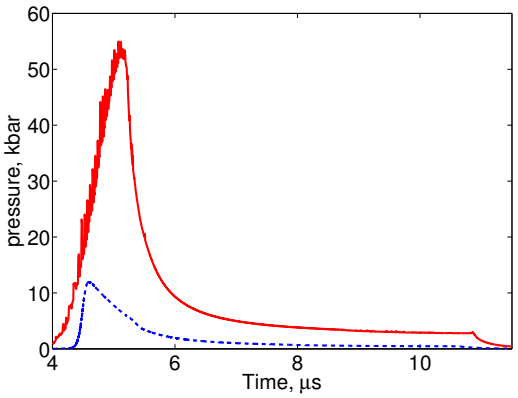

Figure 19: (Color online) Evolution of maximum pressure of case 6 of Table II in [14] by using plasma EOS (red solid line) and polytropic EOS (blue dashed line).

purpose of comparison of our results with [14]. To investigate the dependence of the liner self-collapse pressure on more realistic longitudinal density profile of the liner, we initialize the liner at the PLX chamber wall (R = 137.2 cm) by keeping the liner mass, thickness, velocity and temperature unchanged. When the liner propagates from the chamber wall to the merging radius, its density profile significantly differs from the step-function. Studying liners with such a longitudinal density profile is justified by the fact that single jets traveling from the chamber wall to the merging radius also spread out in both longitudinal and transverse directions. This smoothed longitudinal density profile will then be inherited by a liner obtained by the merger of jets. The plot of density profiles of two liners (see Figure 20(a)) shows that the maximum density in the liner center is close to the initial value of the previous liner but the the leading edge is smoothed out. As a narrow layer adjacent to the liner edge is mostly responsible for the compression, this greatly affects the stagnation pressure. The liner traveling from the chamber edge created the stagnation pressure of only 106.6 bar, a factor of 8.7 decrease compared to the liner traveling from the merging radius (see Figure 21). The corresponding profiles of pressure of two liners at stagnation time are shown in Figure 20(b).

Finally we evaluate the importance of the heat conduction on the argon liner self-implosion. We use the Spitzer electronic thermal conductivity

$$k = k_0 T^{5/2},$$

where the electron temperature is in eV units and the constant

$$k_0 = \frac{3.10275 \times 10^4}{ln\Lambda} \left(\frac{\delta}{\bar{Z}} \right)$$

has the units of $\mathrm{J}/(\mathrm{s} \cdot \mathrm{m} \cdot \mathrm{eV}^{7/2})$, so that the heat flux has the units of $\mathrm{J}/(\mathrm{s} \cdot \mathrm{m}^2)$. Here $\bar{Z}$ is the average charge state of the ions, the Spitzer-Harm coefficient δ depends on $\bar{Z}$: $\delta = 1, 1.582, 2.28, 3.515$, and 4.444, for $\bar{Z} = 1, 2, 4, 16$, and ∞, respectively, and $ln\Lambda \sim 10$. Figure 22 shows the average pressure of the PLX1 liner with and without the thermal conduction. We conclude that the thermal conduction has negligibly small effect in the low-energy PLX regime.

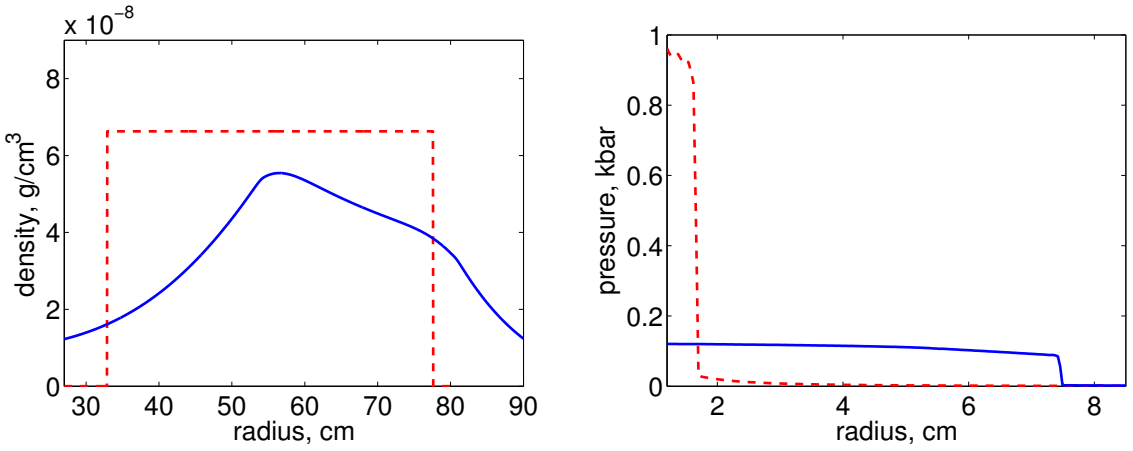

(a) (b)

Figure 20: (Color online) Comparison of density distribution around the merging radius (a) and pressure distributions around the stagnation time (b). One liner was started from the edge of the chamber (blue solid line) and the other liner was initialized at the merging radius (red dashed line).

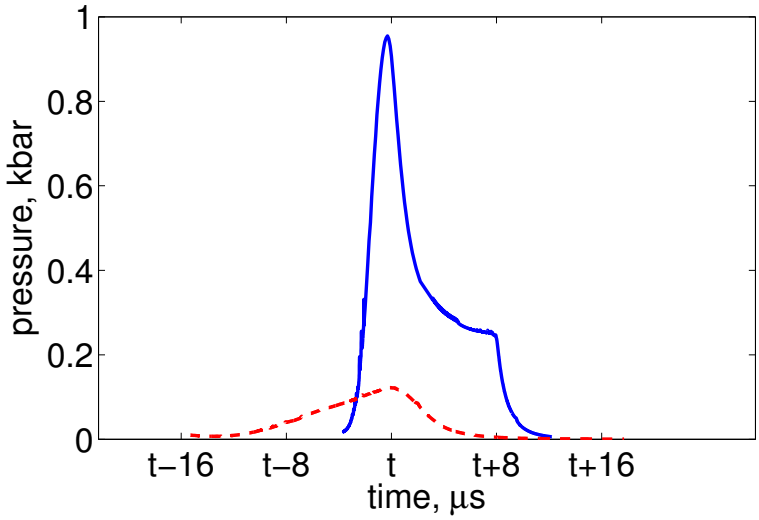

Figure 21: (Color online) Evolution of the maximum pressure near the stagnation time for the self-collapse of the liner initialized at the chamber wall (red dashed line) and at the merging radius (solid blue line). The time axis is shifted to the stagnation point to accommodate different liner arrival times.

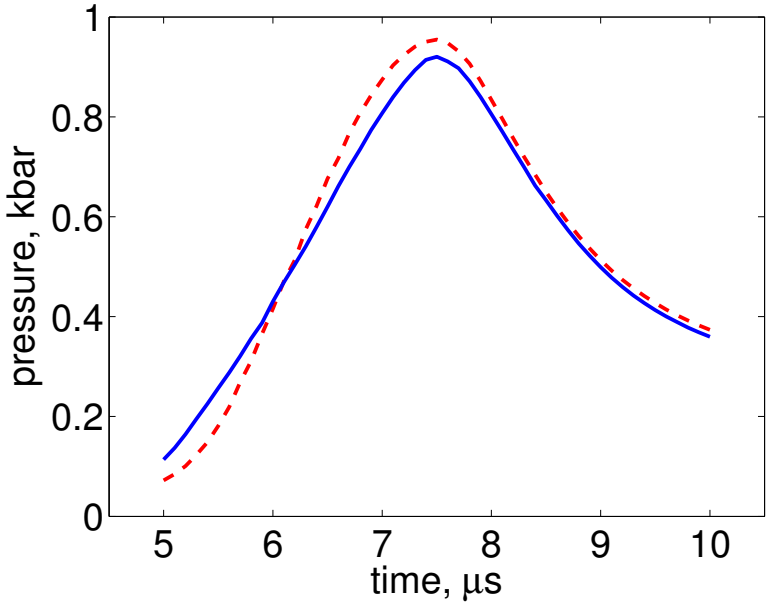

Figure 22: (Color online) Distribution of average pressure of the PLX1 liner without thermal conduction (blue solid line) and with thermal conduction (red dashed line) at the moment of stagnation.

2.3.2 Implosion of liners on plasma targets

In this section, we study the influence of atomic processes in deuterium liners and argon liners on the liner implosion and the efficiency of the target compression. The implosion of high Mach number liners and the compression of targets was studied numerically in [1] using the method of front tracking and the polytropic gas equation of state for deuterium. Within these approximations, [1] showed that deuterium-tritium targets, compressed by deuterium liners, achieved the maximum temperature just above the ignition temperature of 10 keV in the target center producing the fusion energy gain much smaller than unity. Significant fusion energy gain was achieved in [1] only by using heavy xenon liners. In this paper, we re-examine the implosion of deuterium liners using the deuterium EOS model and compare with results obtained by neglecting atomic processes. We also present simulations of imploding argon liners on plasma targets using the argon EOS model. The energy regimes are consistent with the previous work [1] and go beyond liner energies to be used in the PLX experiment.

The initial simulation parameters for deuterium liners, consistent with [1], are as follows. A 5 cm thick deuterium liner has the initial inner radius of 60 cm which corresponds to the merging radius of plasma jets forming the liner. The initial state of the liner is uniform with the density $\rho = 3.8\times10^{-5}\,\mathrm{g/cm^3} = 9.2\times10^{18}\,1/\mathrm{cm^3}$, temperature $T = 0.0358\,\mathrm{eV} = 415.4\,\mathrm{K}$, pressure $P = 0.65\,\mathrm{bar}$, velocity $v = 100\,\mathrm{km/s}$, and the Mach number $M = 60$. The total energy stored in the liner is 164 MJ. Because of the low temperature, we assume that the deuterium in the liner is initially in molecular state. While a plasma jet leaves the plasma gun fully dissociated and

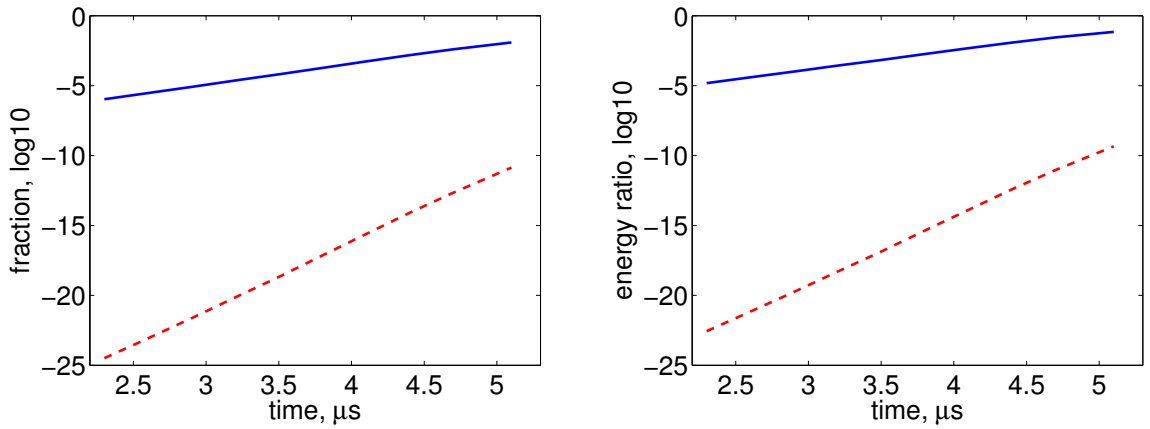

(a) (b)

Figure 23: (Color online) Evolution of atomic processes in the liner before the interaction with the target at given time. (a) Mean dissociation fraction (blue solid line) and ionization fraction (red dashed line) of the liner (b) Mean dissociation energy ratio (blue solid line) and mean ionization energy ratio (red dashed line) of the liner.

ionized, the process of neutralization is very rapid. By integrating the recombination balance equation, we also found that jets will consist of mostly diatomic molecules by the time they reach the merging radius. The plasma target is initially 5 cm in radius, and its initial uniform density and temperature of $\rho = 8.3 \times 10^{-6}\,\mathrm{g/cm^3} = 2 \times 10^{18}\,1/\mathrm{cm^3}$ and $T = 100\,\mathrm{eV}$ correspondingly. Assuming the complete ionization, the initial target pressure is $P = 640.3\,\mathrm{bar}$.

Figure 23(a) shows the evolution of mean dissociation and ionization fractions of deuterium during the liner implosion before the interaction with the target. A mean fraction value is obtained by averaging values across the liner at each time step. The fractions increase with time as the temperature increases. At the late implosion stage, the mean dissociation fraction reaches 0.02 while the ionization fraction remains negligible. Considering small changes of the temperature during the liner implosion (small fractions of eV, see Figure 24(a)) and values of the deuterium dissociation (4.48 eV) and ionization (13.6 eV) energy, this small increase of the dissociation and ionization fractions is easily understood.

To evaluate the importance of the energy sinks by atomic processes, we plot the dissociation and ionization energy ratios defined as the the dissociation (ionization) energy divided by the specific internal energy at given time. Figure 23(b) shows the change of these energy ratios before the interaction with the target. We observe that the dissociation energy constitutes a significant fraction of the liner energy before the interaction with the target while the ionization energy is negligible. The dissociation energy sink causes a large difference of temperature of deuterium liner shown in figure 24(a). The temperature before the interaction with the liner is about 3 times smaller compared to the simulation with polytropic EOS. The corresponding Mach number increases approximately by the factor of two. The evolution of the mean Mach number during the implosion process before the interaction with the liner is shown in Figure 24(b).

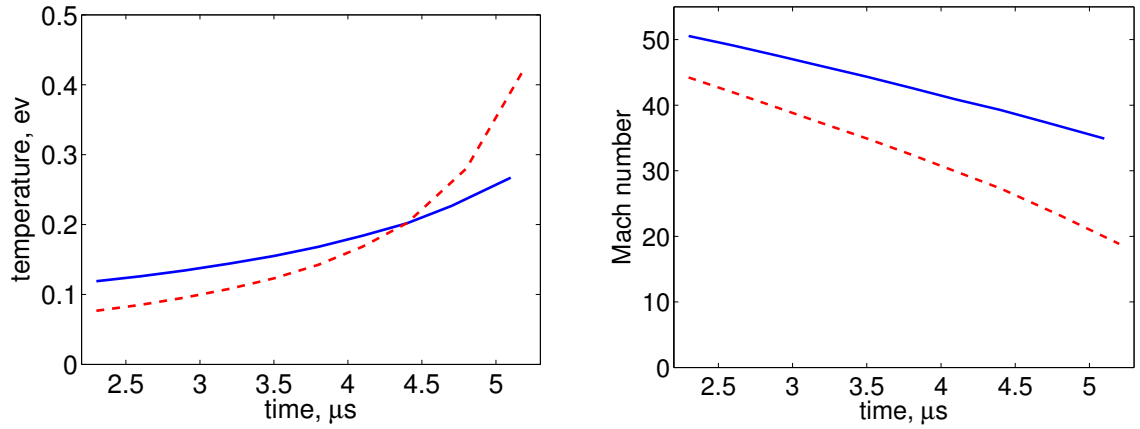

(a) (b)

Figure 24: (Color online) Evolution of the mean temperature (a) and mean Mach number (b) of the liner before the interaction with the target by the plasma (blue solid line) and polytropic (red dashed line) EOS models.

As the liner compresses the plasma target, the ionization processes become important. At stagnation, the front layer of the liner with the thickness of 5 mm becomes completely dissociated and almost completely ionized, with the ionization energy ratio exceeding the dissociation energy ratio (see Figure 25). The profiles of temperature and Mach number in the liner at the moment of stagnation and their comparison with the corresponding simulations using the polytropic EOS are shown in Figure 26.

In agreement with previous theoretical and numerical estimates of scaling laws, the increase of the Mach number leads to much larger compression of the target. Figure 27 depicts the evolution of the maximum pressure in the target after the interaction with the liner. At the target stagnation, the target pressure reached 18 Mbar in the plasma EOS simulation vs. 12 Mbar in the polytropic EOS case. However, atomic processes had no positive effect on the target deconfinement time defined in [11] as the time during which the pressure in the target decreases by the factor of two compared to the fully compressed state.

The increased stagnation pressure and temperature in the target had significant effect on the nuclear fusion gain obtained in simulations using the following approach. At each time step, the production of fusion neutrons was calculated for each computational cell of the target based on the thermodynamic state of the target and the fusion reactivity [7]

$$< \sigma v >= c_1 \theta(T) \sqrt{\frac{\left[BG^2/(4\theta(T))\right]^{1/3}}{D\,T^3}} \exp\left[-3\left[BG^3/(4\theta(T))\right]^{1/3}\right], \tag{23}$$

where

$$\theta(T) = \frac{T}{1 - \frac{T(c_2+T(c_4+Tc_6))}{1+T(c_3+T(c_5+Tc_7))}}.$$

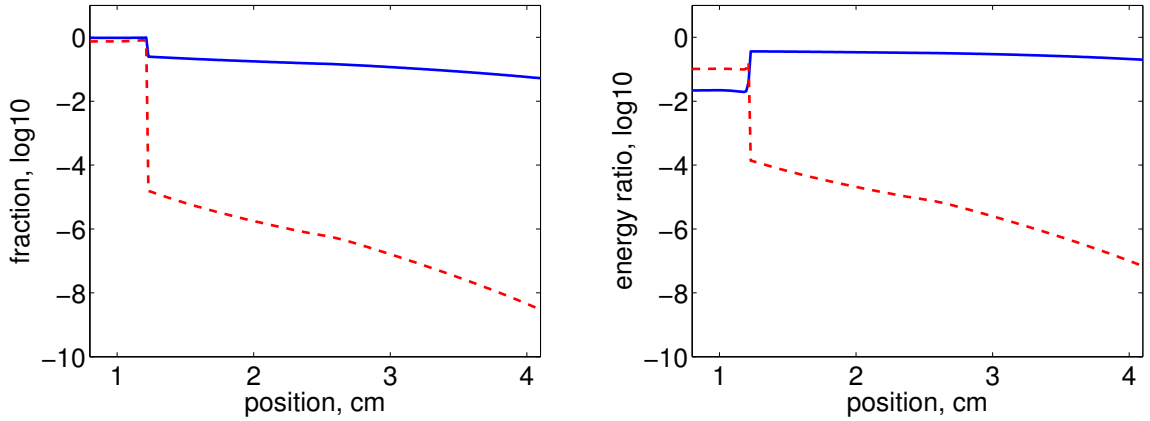

(a) (b)

Figure 25: (Color online) Values of dissociation and ionization fractions, and the corresponding energy ratios across the liner around the stagnation time. (a) Dissociation (blue solid line) and ionization (red dashed line) fractions, (b) Dissociation (blue solid line) and ionization (red dashed line) energy ratios.

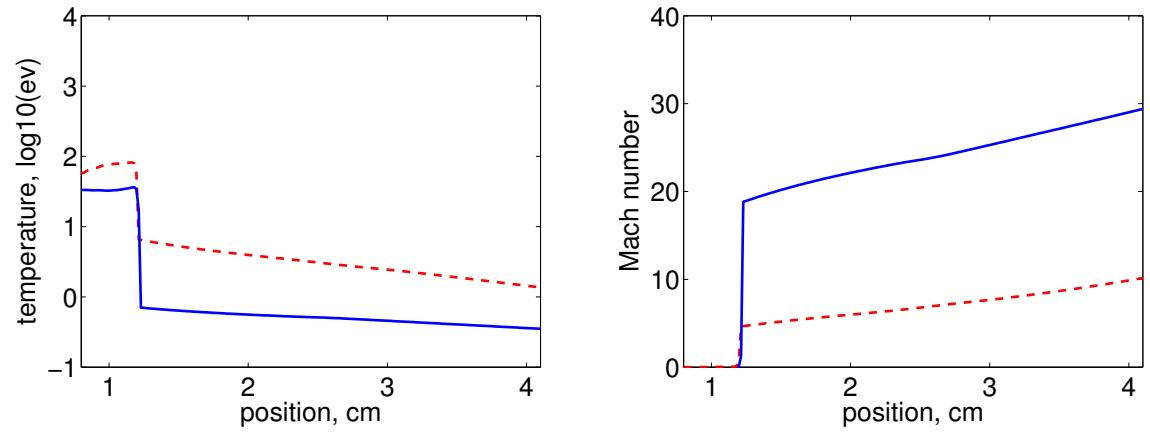

(a) (b)

Figure 26: (Color online) Temperature (a) and Mach number (b) across the liner around the stagnation time by plasma (blue solid line) and polytropic (red dashed line) EOS models.

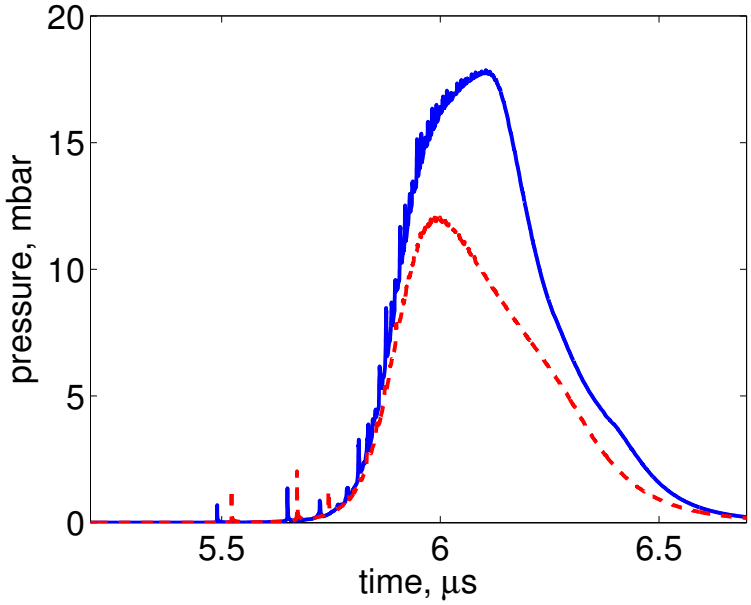

Figure 27: (Color online) Evolution of maximum pressure with polytropic EOS (red dashed line) and plasma EOS (blue solid line) of deuterium liner at given time.

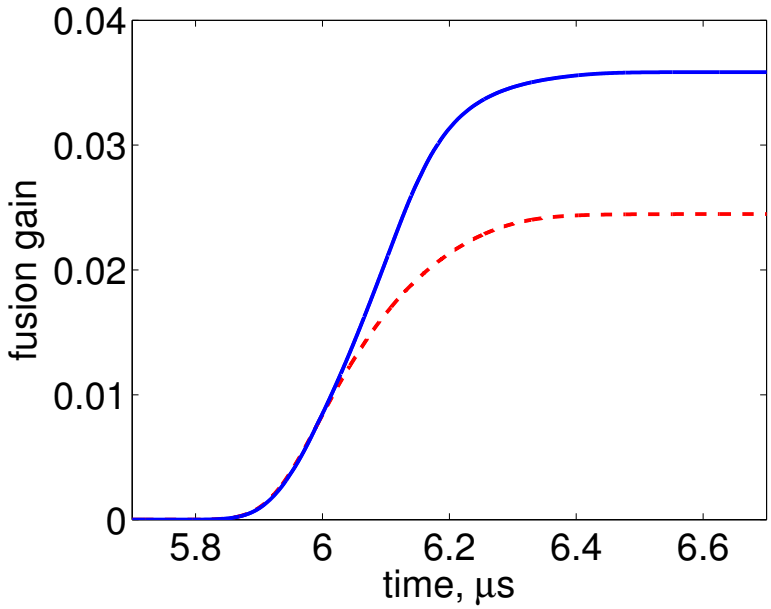

Figure 28: (Color online) Evolution of the fusion energy of the plasma target compressed by the deuterium liner at given time with polytropic EOS (red dashed line) and plasma EOS (blue solid line).

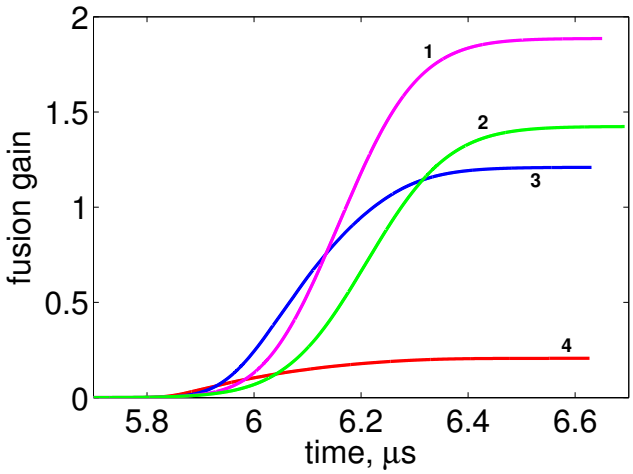

Figure 29: (Color online) Comparison of fusion gains with different target radius using same argon liner and polytropic EOS. (target radius: 15cm(1), 20cm(2), 10cm(3), 5cm(4))

Here the temperature T is in keV units, the dimension of the fusion reactivity is cm^3/s, and coefficients have the following numerical values $c_1 = 1.17302 \times 10^{-9}$, $c_2 = 0.0151361$, $c_3 = 0.0751886$, $c_4 = 0.00460643$, $c_5 = 0.0135$, $c_6 = -1.0675 \times 10^{-4}$, $c_7 = 1.366 \times 10^{-5}$, $BG = 34.3827$, $D = 1.124656 \times 10^6$. The neutron production was integrated in the target volume and time to obtain the total fusion energy

$$E_{\text{fusion}} = (e_{\text{neutron}} + e_\alpha) \int_{t_0}^{\infty} \int\int\int_{V_{target}(t)} < \sigma v > \frac{n^2}{4}\, dV\, dt, \tag{24}$$

where n is the target number density, $e_{\text{neutron}} = 14.1$ MeV is the neutron energy and $e_\alpha = 3.5$ MeV is the alpha particle energy released in the process of fusion. Finally, the fusion gain was obtained as

$$G_{\text{simulation}} = E_{\text{fusion}}/E_{\text{liner}}, \tag{25}$$

where

$$E_{\text{liner}} = E_{\text{kinetic}} + E_{\text{internal}} \simeq E_{\text{kinetic}}$$

is the total initial energy of the plasma liner. Atomic processes contributed to approximately 1.5 times increase of the fusion energy gain, as shown in Figure 28. A simplified alpha-particle heating model was introduced in [1] but not used in the present work. As the production of neutrons and alpha-particles is very small for the case of deuterium liners (the fusion gain is much smaller the unity), the capture of alpha particles by the target can not significantly affect the target state: only 4.3% increase of the fusion gain due to alpha-heating was obtained in [1] for the equivalent liner-target problem. Because of similarly small increase due to alpha-heating in the plasma EOS simulations, we neglected the alpha-heating effect in this work.

As the local thermodynamic equilibrium is an important assumption of the deuterium EOS model, we evaluated it's applicability by analyzing thermodynamic states in the deuterium liner.

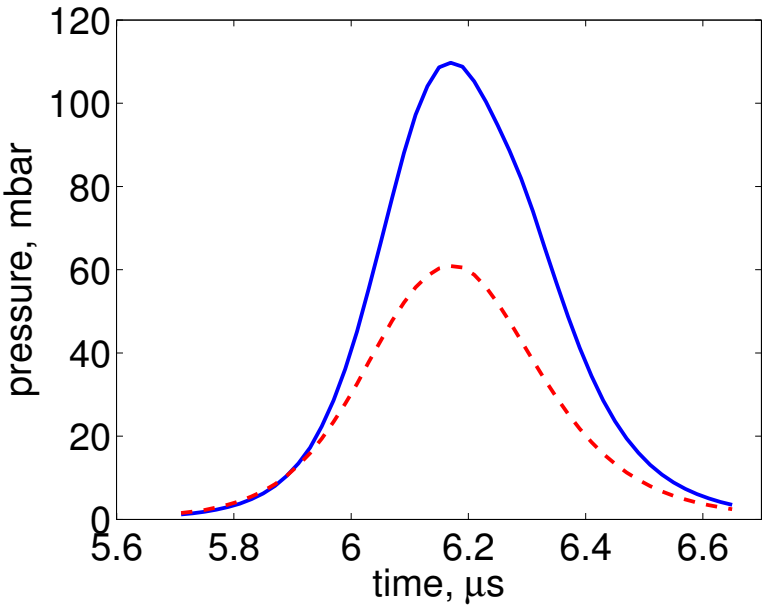

Figure 30: (Color online) Evolution of maximum pressure with polytropic EOS (red dashed line) and plasma EOS (blue solid line) of argon liner at given time.

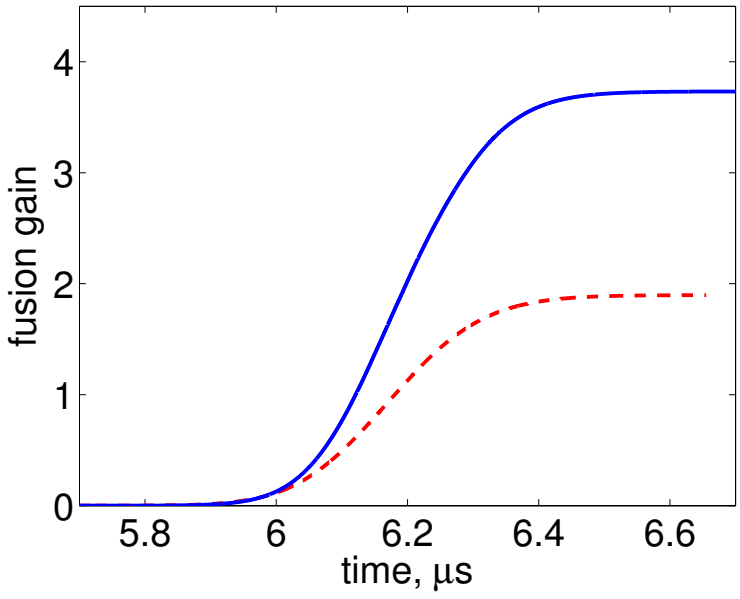

Figure 31: (Color online) Evolution of the fusion energy of the plasma target compressed by the argon liner at given time with polytropic EOS (red dashed line) and plasma EOS (blue solid line).

As the ionization fraction is almost constant and negligibly small during the liner implosion, we consider states of the liner close to the stagnation time, when the ionization is large and rapidly changing in time. To achieve the thermodynamic equilibrium in such a dynamic process, two conditions must be satisfied [15]. The first condition, applicable to processes at both fast and slow time scales, requires the electron number density to be higher than a critical value defined as

$$n_e \geq 7.4 \times 10^{18} \frac{z^7}{n^{17/2}} \left(\frac{kT}{E_i^z} \right)^{1/2} \; [cm^{-3}],$$

where $z = 1$ for neutrals, $z = 2$ for singly ionized atoms etc., n is the principal quantum number, and E_i^z is the ionization energy. The value of critical electron number density is 1.15×10^{19} for temperatures close to the stagnation point. The actual number density of electrons according to the ionization fraction from EOS is 1.3×10^{23}, or four orders of magnitude higher. While the formula above sometimes is used for high-Z materials, it is applicable, strictly speaking, only to hydrogen and helium. The second condition defines a typical time scale for reaching the equilibrium in transient plasmas:

$$\tau \simeq \left[3 \times 10^{-7} \left(\frac{E_i}{kT} \right)^{3/2} n_e \right]^{-1} \frac{n}{n_a} \frac{M}{m} \; [sec].$$

Close to stagnation, the time scale given by this expression is $1.6 \times 10^{-12} sec$. This is approximately two times smaller than the smallest time step used during the simulation. Therefore the local thermodynamic equilibrium is established on shorter time scales than the resolved hydrodynamic time scale. This proves the applicability of our LTE EOS model.

The next problem we consider is the compression of plasma targets by heavy argon liners. We use the same liner dimensions as in [1] and the same liner particle number density as in previous simulations with xenon liners. This gives the following initial state of the argon liner: density $\rho = 4.0 \times 10^{-4}\,\mathrm{g/cm^3} = 6.03 \times 10^{18}\,1/\mathrm{cm^3}$, temperature $T = 0.7269\,\mathrm{eV} = 8435.15\,\mathrm{K}$, and pressure $P = 9.35\,\mathrm{bar}$. [1] explained that heavy, high-Z liners over-compress small targets used for the deuterium liners and found that the most optimal target radius for the given xenon liner is 20 cm. Similarly, we find first the most optimal target size for the argon liner by using several target radius and the polytropic EOS model. Results depicted in Figure 29 show that the target with the radius of 15 cm is the most efficient with respect to the fusion gain. This target size is then used for the investigation of the influence of ionization on the target stagnation pressure and fusion energy gain. The target stagnation pressure of 61 Mbar, obtained by neglecting the liner ionization via the polytropic EOS, increased to 110 Mbar when the argon EOS with ionization was used.(Figure 30) The corresponding numbers for the fusion energy gain were 1.9 and 3.7, correspondingly.(Figure 31)

2.4 Conclusion

We have investigated the influence of atomic physics processes on the implosion of deuterium and argon liners for magneto-inertial fusion via numerical simulations in spherically symmetric geometry. Simulations used the front tracking code FronTier designed to accurately handle

material interfaces or multiphase systems with large discontinuities in solutions or system properties. FronTier solutions involving strong radial shocks were verified using analytical solutions of the spherically symmetric Noh problem. A good agreement with the theory and the second order convergence was observed, and the comparison with identical verification tests of [14] was performed. FronTier outperformed the Raven and SPH codes and showed identical accuracy to the HELIOS code. We would like to note that the described simulations test only the ability of interior solvers of the FronTier code to deal with strong radial shocks. The accuracy of FronTier for tracking contact discontinuities exceeds the accuracy of interior solvers. This feature is critical for the simulation of tracked target boundaries in the PJMIF simulations.

The equation of state models for deuterium and argon, valid in the approximation of local thermodynamic equilibrium, include processes of dissociation (for molecular deuterium) and ionization. The applicability of the local thermodynamic equilibrium approximation to the plasma liner problem has also been verified. The numerical EOS software for argon, built upon ideas of the average ionization model by Zeldovich, was verified using accurate solutions of the coupled system of Saha equations.

Parameters of the planned Plasma Liner Experiment at Los Alamos were used for the simulation of self-collapse of argon liners. For the purpose of comparison with [14], the liner was initialized in the first series of simulations at the merging radius of 33 cm. The liner ionization contributed to the cooling of the liner during the implosion (before the self-collapse) and the 1.5 times increase of the Mach number. At the moment of stagnation, ionization reached the level of 7.2 in the leading edge of the liner and contributed to the 6.5 times increase of density in the implosion center and the doubling of pressure. With ionization, the stagnation pressure reached 930 bar for the set of initial parameters denoted as PLX1 and PLX2. The maximum stagnation pressures achieved in our simulations were approximately three order of magnitude smaller compared to [14], which included radiation transport but no ionization. FronTier results obtained with LTE plasma EOS were comparable to those obtained by the HELIOS code with the PROTACEOS non-LTE EOS in [14]. Ionization did not have any effect on the target deconfinement and stagnation times. However a significant decrease of the stagnation pressure (8.7 times) was observed when the liner traveled from the edge of the chamber (137.2 cm) caused by the longitudinal spread of the liner density, especially near the leading edge. Our studies showed that the thermal conduction in the liner has negligible effect on the main characteristics of the self-implosion of PLX liners.

Simulations of deuterium liners compressing deuterium targets showed that while the dissociation and ionization fractions remained very small during the implosion process prior to the collision with the target, the energy used for dissociation contributed to the reduction of temperature and the increase of the Mach number by approximately the factor of two. The ionization energy remained negligible before the interaction with the target. During the target compression, the leading edge of the liner became significantly ionized and the ionization energy overcame the dissociation energy. Atomic processes contributed to the increase of the stagnation pressure from 12 Mbar (simulations with the polytropic EOS) to 18 Mbar (plasma EOS) and to approximately 1.5 times increase of the fusion energy produced by the plasma target.

Similar results were obtained in simulations of argon liners compressing plasma targets. The initial radius of the plasma target compressed by the heavier argon liner was optimised first to achieve the maximum fusion energy gain. Using the optimum target size of 15 cm, the influence

of ionization in the liner on the target compression was investigated. Ionization contributed to the doubling of the stagnation pressure in the target and the fusion energy gain.

3 3D Simulations of Plasma Jet Merger and Formation and Implosion of Plasma Liners

3.1 Summary

The internal structure and self-collapse properties of plasma liners, formed by the merger of argon plasma jets, have been studied via 3-dimensional numerical simulations using the FronTier code. We have shown that the jets merger process is accomplished through a cascade of oblique shock waves that heat the liner and reduce it's Mach number. Oblique shock waves and the adiabatic compression heating have led to the 10 times reduction of the self-collapse pressure of a 3-dimensional argon liner compared to a spherically symmetric liner with the same pressure and density profiles at the merging radius. We have also observed a factor of 10 variations of pressure and density in the leading edge of the liner along spherical surfaces close to the interaction with potential plasma targets. Such a non-uniformity of imploding plasma liners presents problems for the stability of targets during compression. This Section is based on [3].

3.2 Cylindrically symmetric simulation of detached argon jet

In this section, we present simulation results of the propagation of a single detached argon plasma jet from the nozzle of the plasma gun to the merging radius. The purpose of this simulation is to calculate the distribution of density and pressure in the plasma jet before the merger to be used as input data for 3-dimensional jet-merger simulations. In this study, we use PLX case 6 of Table 2 in [14], which has the following constant states: initial velocity 50 km/s, the density $\rho = 5.747 \times 10^{-6} g/cm^3$, and the temperature $T = 1eV$. The ambient vacuum is modeled as rarefied gas with density $\rho_0 \sim 10^{-9} g/cm^3$ and pressure $\sim 10^{-6}$ bar. We assume that the jet remains axially symmetric during the expansion and use a 2-dimensional cylindrically symmetric domain with open boundary conditions.

Figure 32 shows the distribution of the initial density in the detached jet and the density profile at $t = 18.5\mu s$ or at 0.925m distance from the plasma gun nozzle. Profiles of density, pressure, temperature and average ionization in the transverse direction through the jet center at different moments of time are shown in Figure 33. We observe that the all quantities decrease in time and the jet boundary quickly becomes very diffuse. In order to preserve the notion of the expanding jet radius, we define it as the location of points with the density of $0.1\rho_0$.

The jet expansion can also be estimated analytically. The liner expansion model with constant initial sound speed [8] predicted the increase of the jet radius b as $b(r_m) = b_0 + c_0(r_c - r_m)/u_j$. Here b_0 is the initial jet radius, c_0 is the initial sound speed, r_c is the chamber radius, and r_m is the merging radius.

The linear expansion model can be improved if we assume that the jet expands adiabatically and the sound speed decreases accordingly during the expansion:

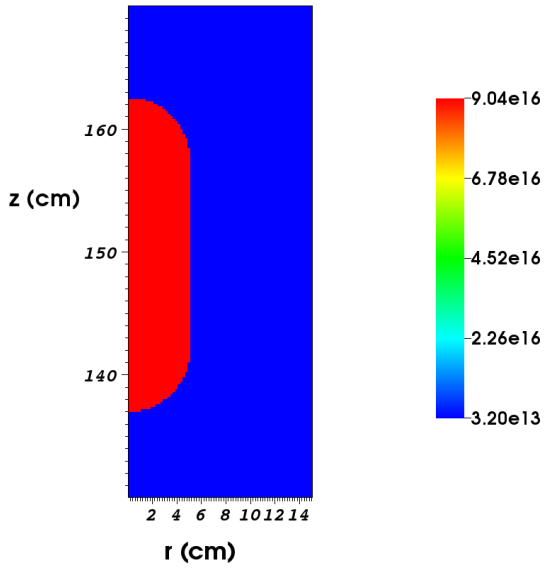

(a) t = 0.0 ms

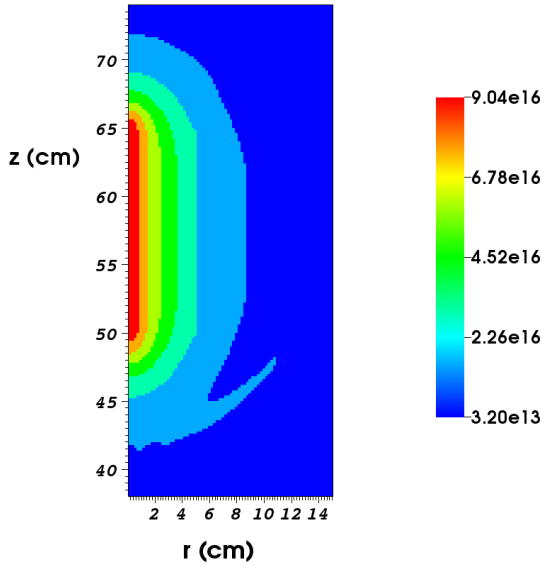

(b) t = 0.0185 ms

Figure 32: (Color online) Density ($1/cm^3$) of the detached jet. (a): initial density; (b): density before merging radius.

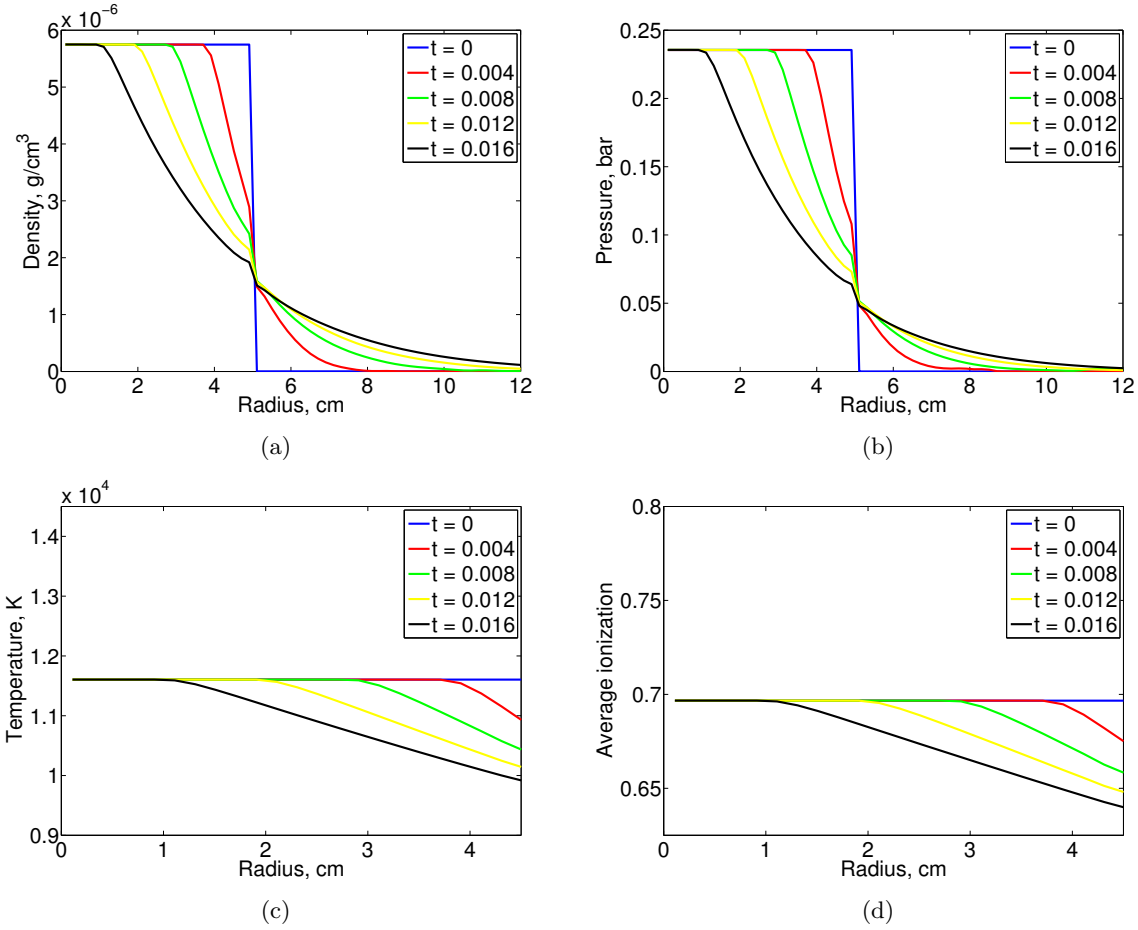

Figure 33: (Color online) Density, pressure, temperature and average ionization across the center of the detached argon jet.

$$c(t) = \sqrt{\gamma \frac{P(t)}{\rho(t)}} = \sqrt{\gamma A \rho(t)^{\gamma-1}},$$

where A is the constant in the adiabatic relation $P = A\rho^{\gamma}$. If the jet length is much longer than the jet diameter, we obtain

$$b(t) = b_0 + c_0 \left(\frac{b_0}{b(t)} \right)^{(\gamma-1)} t.$$

If the jet length is comparable to the diameter, we can assume spherical expansion and obtain

$$b(t) = b_0 + c_0 \left(\frac{b_0}{b(t)} \right)^{\frac{3}{2}(\gamma-1)} t.$$

For $\gamma = 5/3$, we obtain the following nonlinear equation for a long cylindrical jet

$$[b(t)]^{2/3} (b(t) - b_0) = c_0 b_0^{2/3} t \tag{26}$$

and the quadratic equation for a short spherical jet

$$[b(t)]^2 - b_0 b(t) - c_0 b_0 t = 0. \tag{27}$$

For simulations using the argon plasma EOS, we calculate the local gamma $\gamma = 1.14$ and solve numerically the corresponding nonlinear equations. Figure 34 depicts the time dependence of the expanding jet radius from simulation and analytic model.

In view of the importance of high values of the Mach number for achieving high values of the self-implosion pressures or high target compression rates, we are especially interested in the Mach number change during the jet expansion. Before presenting numerical results on the Mach number increase during the adiabatic cooling process, we need to justify our method of data selection. A very strong rarefaction wave behind the detached jet affects the Mach number at the tail of the jet. If we include the jet tail data to calculate the average Mach number, large values of the Mach number in vacuum behind the jet tail will significantly raise the average Mach number. Therefore we only consider the front half of the jet body when we calculate the average Mach number from the numerical data.

Figure 35 shows the jet cooling during the process of expansion. The average Mach number increases with time and reaches the value of 26 and the average temperature decreases with time. As expected, the increase of the jet length slightly increases the average Mach number after the expansion.

3.3 Merger of 30 argon jets and oblique shock waves

In this section, we examine the structure of the liner obtained by the merger of plasma jets, the liner uniformity, the reduction of the Mach number during the liner implosion, and compare with the theory of oblique shock waves. To evaluate the degradation of 3-dimensional plasma

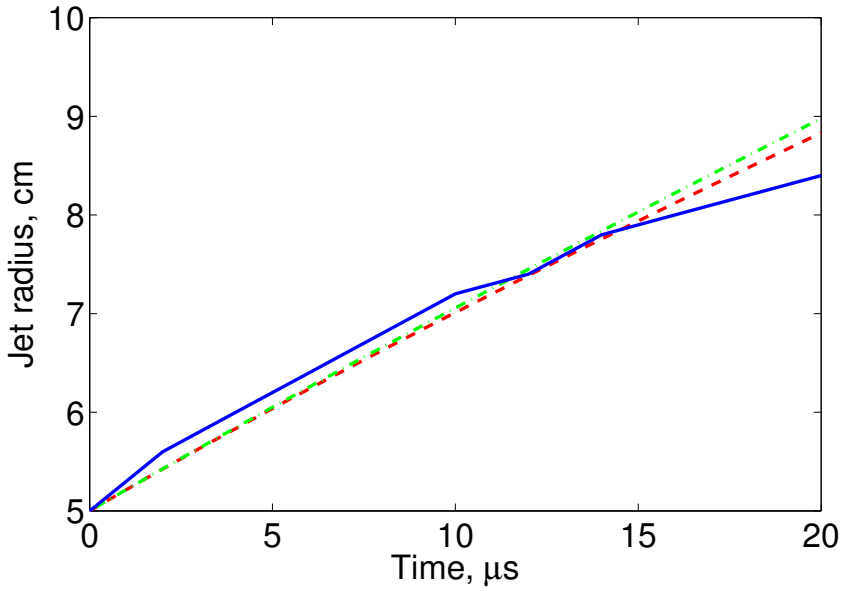

Figure 34: (Color online) Jet expansion comparison of numerical simulation result (blue solid line), analytic model of long jet (green dash-dotted), and analytic model of short jet (red dashed line).

liner abilities to compress targets due to oblique shock waves, we compared our results with the 1-dimensional spherically symmetric case in the next section.

The 3-dimensional simulation initialization involves (a) finding directions of 30 jets uniformly distributed in space and (b) initialization of states around each direction using pressure, density, and velocity profiles from the 2-dimensional detached jet simulation. The problem (a), equivalent to the uniform distribution of 30 points on a unit sphere, is solved using Spherical Centroidal Voronoi Tessellation (SCVT). The initialization of states is obtained by performing a transformation from 2-dimensional cylindrical coordinate into 3-dimensional cartesian coordinate and using the corresponding numerical data sets with bi-linear interpolation.

The angle between each pair of argon jets is approximately 36 degrees. As jets collide at the merging radius, they can not interpenetrate each other and change their direction via the oblique shock waves. To show this, we evaluate the mean free path of ions. The mean free path of ions in the plasma jet is evaluated [16] as

$$\lambda_i = v_{Ti}/\nu_i, \tag{28}$$

where the ion thermal velocity is $v_{Ti} = 9.79 \times 10^5 \mu^{-1/2} T_i^{1/2}$ cm/s, and the ion collision rate is

$$\nu_i = 4.80 \times 10^{-8} Z^4 \mu^{-1/2} n_i T_i^{-3/2} \ln\Lambda,\ 1/s.$$

Using states of the jet edge from the simulation study, $\mu = m_i/m_p = 40$, $T_i = 0.86$ eV, $Z \sim 1$, $n_i = 1.5 \times 10^{16}\, cm^3$, $\ln\Lambda \sim 10$, we obtain $v_{Ti} = 1.44 \times 10^5$ cm/s, $\nu_i = 1.43 \times 10^9$ 1/s, and

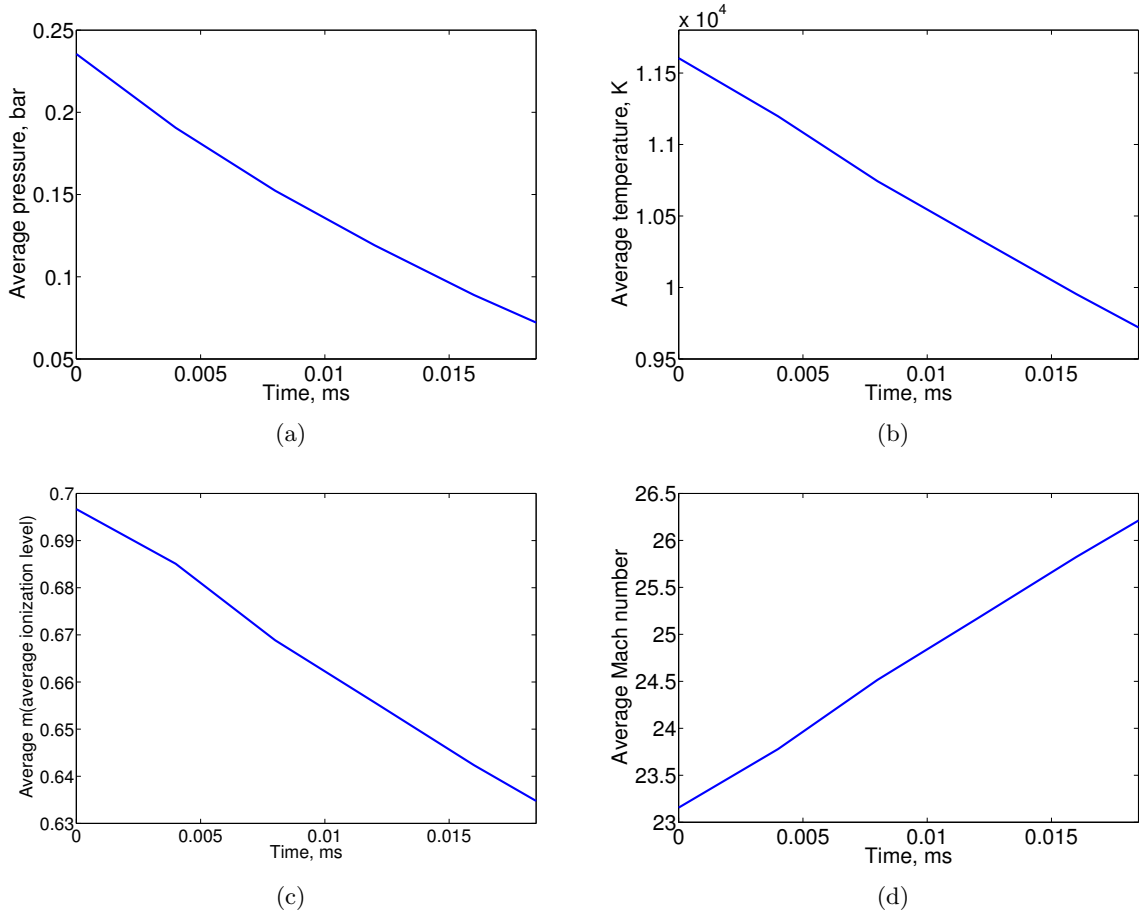

Figure 35: (Color online) Average values of pressure, temperature, m (average ionization) and Mach number of a detached argon jet.

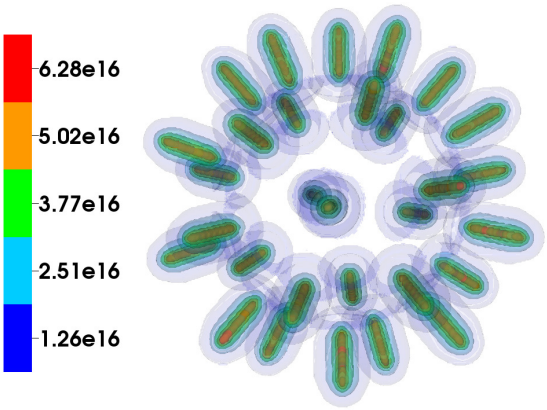

(a) t = 0.0203 ms

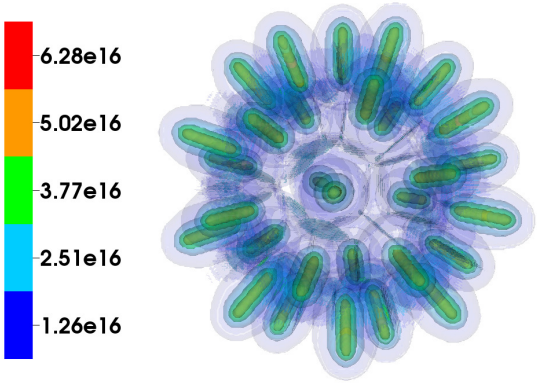

(b) t = 0.0223 ms

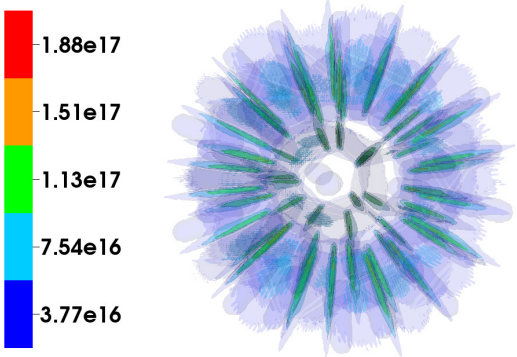

(c) t = 0.0243 ms

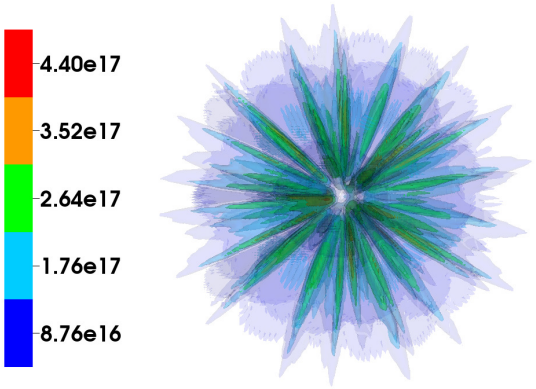

(d) t = 0.0263 ms

Figure 36: (Color online) Density ($1/cm^3$) contours before merger (a, b) and after merger (c, d) of 30 argon plasma jets.

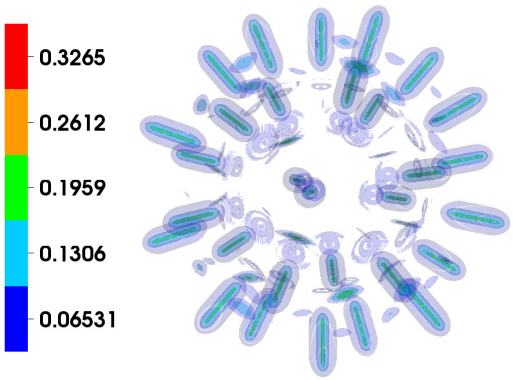

(a) t = 0.0203 ms

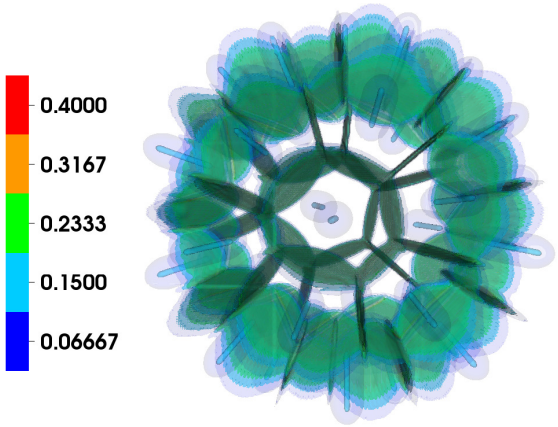

(b) t = 0.0223 ms

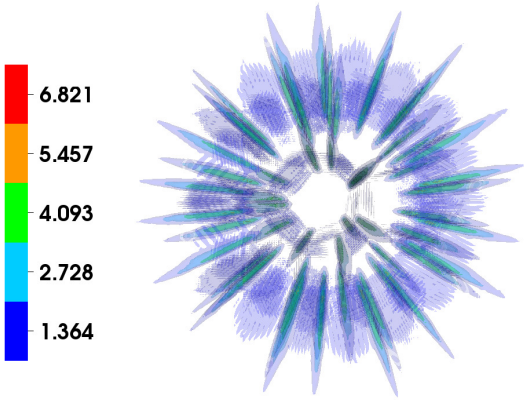

(c) t = 0.0243 ms

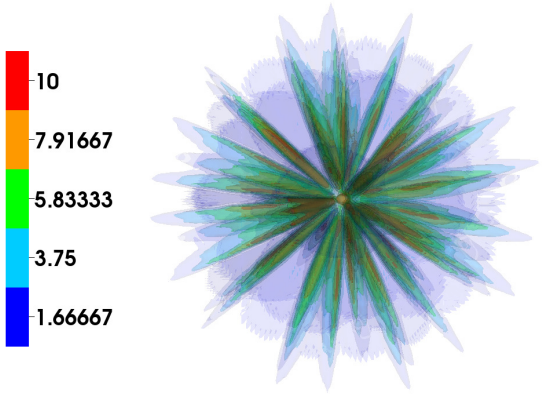

(d) t = 0.0263 ms

Figure 37: (Color online) Pressure (bar) contours before merger (a, b) and after merger (c, d) of 30 argon plasma jets.

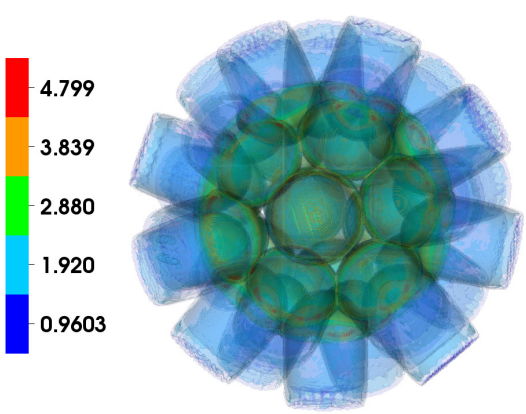

(a) t = 0.0203 ms

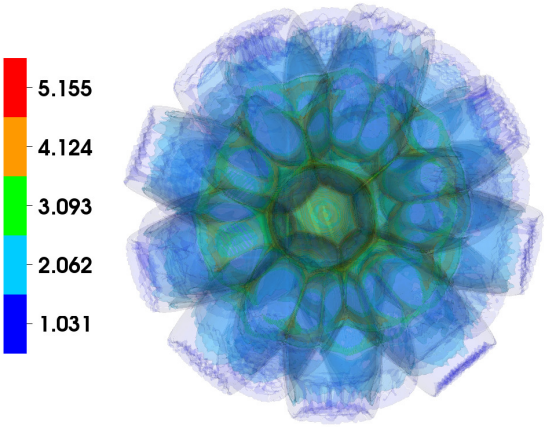

(b) t = 0.0223 ms

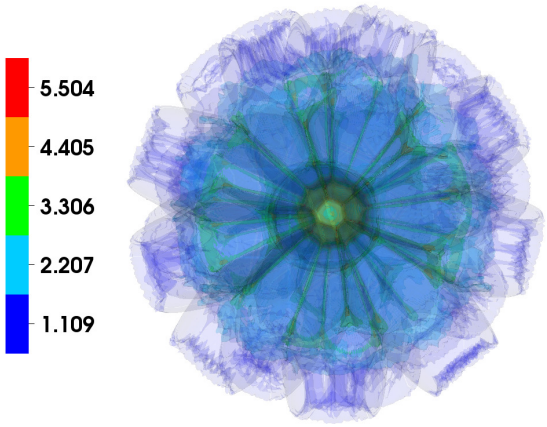

(c) t = 0.0243 ms

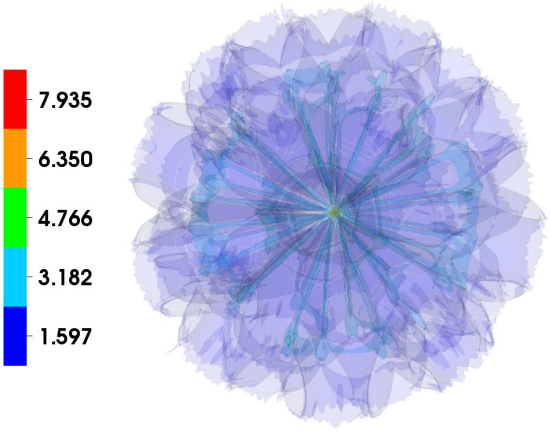

(d) t = 0.0263 ms

Figure 38: (Color online) Average ionization contours before merger (a, b) and after merger (c, d) of 30 argon plasma jets.

$\lambda_i \sim 1 \times 10^{-4}$ cm. Therefore the edge of the jet is fully collisional and the mean free path in the jet center is even shorter. In the case of the jet merger, we integrate numerically the equation describing the slowing down of streaming ions on ion-ion collisions. [16] The slowing down rate is evaluated by using

$$\frac{dv_\alpha}{dt} = -\nu_s^{\alpha\backslash\beta} v_\alpha \tag{29}$$

where $\nu_s^{\alpha\backslash\beta} = (1 + m_\alpha/m_\beta)\psi(x^{\alpha\backslash\beta})\nu_0^{\alpha\backslash\beta}$, $\nu_0^{\alpha\backslash\beta} = 4\pi n_\beta e_\alpha^2 e_\beta^2 \lambda_{\alpha\beta}/m_\alpha^2 v_\alpha^3$, $x^{\alpha\backslash\beta} = m_\beta v_\alpha^2/2kT_\beta$, and $\psi(x) = \frac{2}{\sqrt{\pi}} \int_0^x t^{1/2} e^{-t} dt$. With the parameters in the jet edge and $\lambda_{\alpha\beta} \sim 10$, we obtain that the ion's penetrating velocity ($v_\alpha^{initial} \sim 3.1 \times 10^6$ cm/s) is slowed down to thermal velocity after distance of around 0.5cm. Considering the fact that electrons are indeed highly collisional and the electrostatic interaction will reduce the ion penetration, the single fluid dynamics description of the jet merger process is justified.

Oblique shock waves heat the liner, reduce the average Mach number, and contribute to the liner non-uniformity. Density, pressure average ionization contours before and after merger of 30 jets are shown in Figures 36, 37, and 38. During the jet merger process, the highest pressure appears along the plane of interaction of the neighboring jets. We observe the formation of high pressure contours having shapes of the pentagon and hexagon, depending on the number of jet closest neighbors. This phenomenon was also observed in [17]. Due to oblique shock waves, the highest pressure is located in the middle between jet axes, while the highest density still remains in the main body of jet during initial stages of the jet merger. At later stages, the highest density also shifts to the hexagon- and pentagon- shaped structures located between jet axes. The distribution of density states on a plane slicing of the 3-dimensional computational domain which contains the origin and axes of the neighboring three jets is shown in Figure 39(a).

The schematic of oblique shocks is shown in Figure 39(b). In this figure, δ denotes the angle between the plasma jet and the plane of reflection (the median line between two jets), and α denotes the angle of the oblique shock wave. With respect to the formation of oblique shock waves, the collision of jets is similar to the collision of a jet with a solid wall at 18-degree angle, and therefore the standard theory of oblique shock waves [18] is applicable for the description of states in the after-shock region of the jet merger process. Assuming initially non-expanding flow (with parallel stream lines) with polytropic gas properties and $\gamma = 5/3$, the oblique shock wave's angle (α), pressure (P), density (ρ), temperature (T), and Mach number (M) in the after-shock region can be calculated by using following equations:

$$\frac{\tan(\alpha - \delta)}{\tan\alpha} = \frac{2 + (\gamma - 1)M_1^2 \sin^2\alpha}{(\gamma + 1)M_1^2 \sin^2\alpha} \tag{30}$$

$$\frac{P_2}{P_1} = \frac{2\gamma M_1^2 \sin^2\alpha - (\gamma - 1)}{\gamma + 1} \tag{31}$$

$$\frac{\rho_2}{\rho_1} = \frac{(\gamma + 1)M_1^2 \sin^2\alpha}{(\gamma - 1)M_1^2 \sin^2\alpha + 2} \tag{32}$$

$$\frac{T_2}{T_1} = \frac{[2\gamma M_1^2 \sin^2\alpha - (\gamma - 1)][(\gamma - 1)M_1^2 \sin^2\alpha + 2]}{(\gamma + 1)^2 M_1^2 \sin^2\alpha} \tag{33}$$

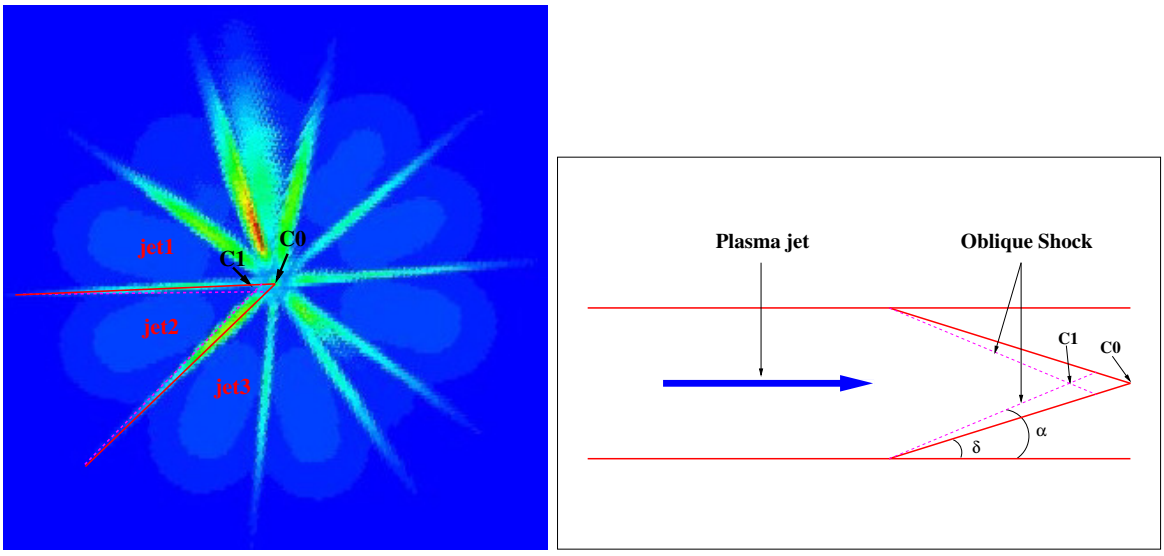

(a) (b)

Figure 39: (Color online) (a) Density distribution on a slice of 3-dimensional data at stagnation and (b) schematic of oblique shocks in the jets merger process.

$$M_2^2 \sin^2(\alpha - \delta) = \frac{(\gamma - 1)M_1^2 \sin^2 \alpha + 2}{2\gamma M_1^2 \sin^2 \alpha - (\gamma - 1)} \tag{34}$$

where quantities with the index 1 describe the pre-shock state and the corresponding quantities with index 2 describe the post-shock state.

For a better explanation of the liner structure and results of 3-dimensional simulations of PLX experimental conditions, we have also performed simplified 2-dimensional simulations of the jet merger in planar geometry using the polytropic gas equation of state and compared with the theory. Other simplifications such as initially uniform distributions of the pressure and density of jets with sharp boundaries (non-expanding jets before the merger) were also used in these idealized 2-dimensional simulations. The angle between jets was close to the corresponding angle in the 3-dimensional jets array. Figure 40 shows the schematic of the process: the initialization of the jet merger simulation and the density distribution at later time exhibiting the first and second cascades of oblique shock waves. The detailed distributions of pressure, density, and Mach number after the formation of the first oblique shock waves are shown in Figure 41. The simulated values of pressure, density, Mach number and other quantities in the post-shock region were compared with solutions of the nonlinear system of oblique shock equations and a good agreement was reached. Results of the comparison are summarized in Table 1. We would like to note that the small discrepancy between the theory and simulation is due to the fact that the theory deals with a steady-state oblique shock while the steady state was not fully reached in the simulation before the second oblique shock followed.

The flow velocity vector after the first shock wave is parallel to the mid-plane between the original gas jets. Therefore the angle between converging flows after the oblique shock waves

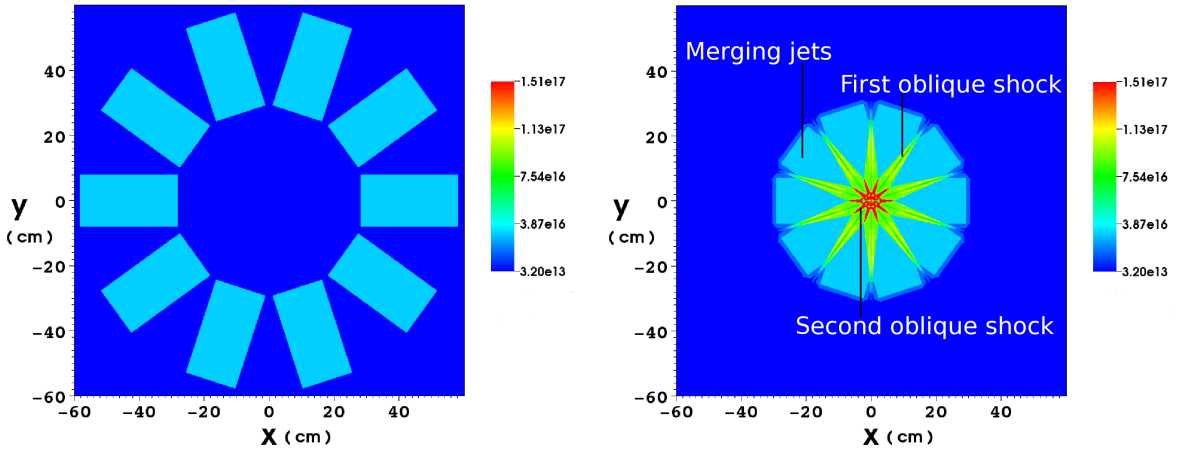

(a) (b)

Figure 40: (Color online) (a) Initial density of the 2-dimensional jet merger simulation and (b) density distribution showing the first and second cascades of oblique shocks. $(1/cm^2)$

	α	M_2	ρ_2/ρ_1	T_2/T_1	P_2/P_1
Theory	24.8	3.9	3.9	35	137
Simulation	23.5	4.0	3.5	35	135

Table 1: Comparison of simulations and theory of states in the first oblique shock wave.

is again 36 degrees and at some distance the flows collide with the formation of a secondary oblique shock wave. This secondary shock is again equivalent to the reflection of the flow by a plane at 18-degree angle. The distributions of states after the formation of the second oblique shock are shown in Figure 42 and the corresponding results of the comparison of theory and simulations are given in Table 2. In idealized case (the absence of the residual vacuum gas in the chamber and the expansion of the leading edge of jets) the cascades of oblique shock waves would continue until the chamber center is reached. We estimate that in the given geometry, the chamber center would be reached after the third oblique shock wave, and the converging flow after the third shock wave will lead to a hammer-shock in the center. But the third oblique shock wave was not clearly visible in simulations due to imperfect conditions mentioned above.

	α	M_2	ρ_2/ρ_1	T_2/T_1	P_2/P_1
Theory	33	2.3	2.4	2.3	5.6
Simulation	30	2.4	2.5	2.3	5.3

Table 2: Comparison of simulations and theory of states in the second oblique shock wave.

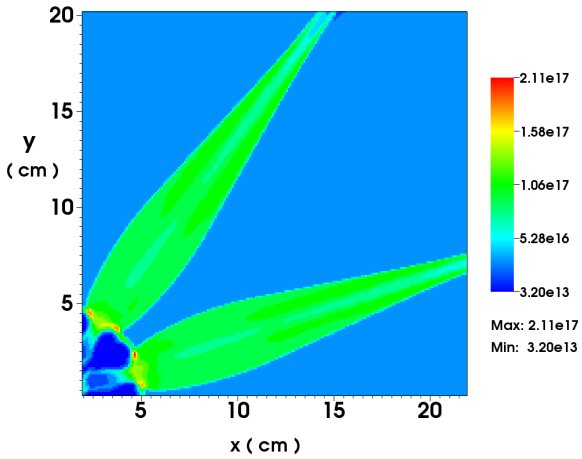

(a) Number density, $1/cm^2$

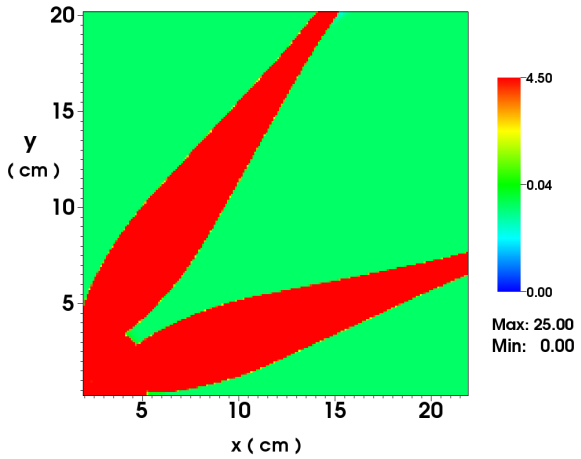

(b) Pressure, bar

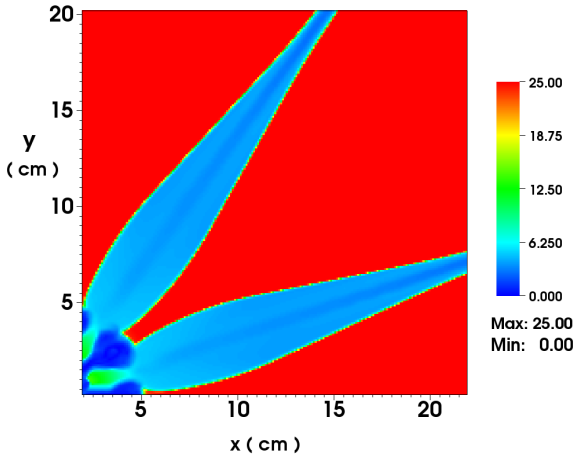

(c) Mach number

Figure 41: (Color online) First cascade of oblique shock waves in 2-dimensional jet merger simulation.

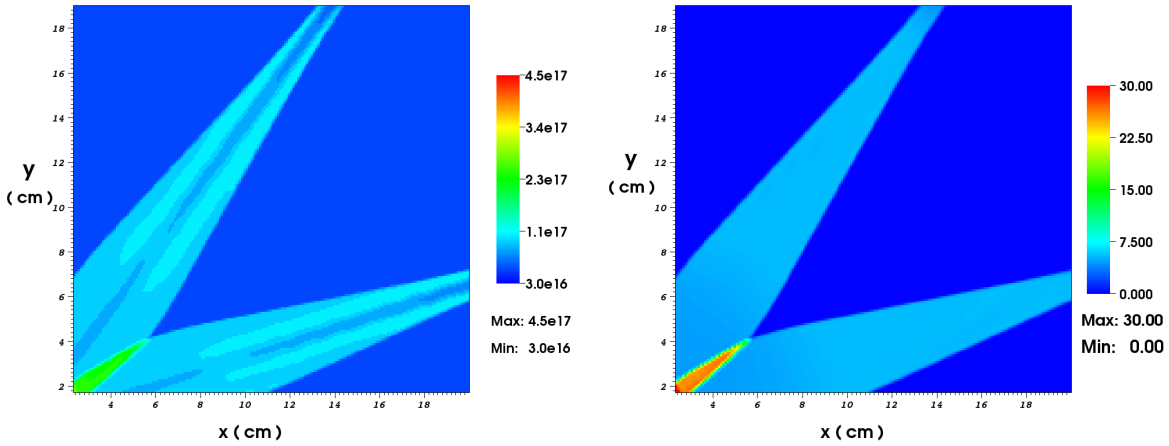

(a) Number density, $1/cm^2$

(b) Pressure, bar

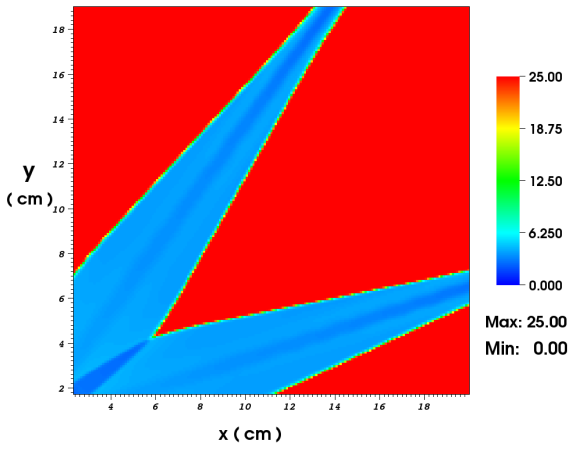

(c) Mach number

Figure 42: (Color online) Second cascade of oblique shock waves in 2-dimensional jet merger simulation.

3.4 3-dimensional liner analysis and comparison with self-implosion of uniform liners

Based on theory and numerical simulations, we conclude that the structure of a plasma liner is a cascade of oblique shock waves generated by merging jets, and if the flow after the last oblique shock wave remains supersonic, it leads to a central hammer shock. Returning now to the main 3-dimensional simulation results, we admit that precise theoretical analysis of the 3-dimensional jets merger is difficult for the following reasons:

- Secondary shocks due to three-jet interactions. The post-shock regions are shown below in Figure 45 on spherical splices of the liner.
- Spreading out of free jets in the longitudinal and transverse directions. We have estimated that at the moment of the jet merger, the outgoing radial velocity of plasma particles equals approximately 6% of the longitudinal velocity. For peripheral layers of plasma jets, this effectively increases the merger angle by 6 degrees and contributes to larger reduction of the Mach number. But as the distribution of states is non-uniform across the merging jets, this effect is less important for interior jet layers.
- Change of the ionization fraction. We observe that the ionization fraction across the first oblique shock wave in the 3-dimensional simulation changes by the factor of 4. Theoretical formulas are derived for constant number of gas atoms (polytropic gas).
- The decrease of the Mach number in the imploding liner is caused not only by oblique shock waves but also by the heating associated with the adiabatic compression.

Rather than attempting an approximate comparison with the oblique shock theory, we analyse 3-dimensional simulation results, average them in radial coordinates, and compare with the corresponding spherically symmetric, 1-dimensional simulations that operate with the same amount and similar distribution of the liner plasma and the residual vacuum gas. Figure 43 depicts the evolution of the averaged Mach number in the 3-dimensional liner formed by the merger of 30 jets and the Mach number of the 1-dimensional liner containing the same amount of mass and having the same pressure and density profile as the profiles of the 3-dimensional jets at the merging radius averaged in radial coordinates. The higher initial value of the average Mach number of the 3-dimensional liner is due to the expansion of free jets prior to their merger, as shown in Section 2, Figure 35(d). After the merger, the Mach number of the 3-dimensional liner reduces faster compared to the 1-dimensional liner, reaching values of 14.4 (3-dimensional) and 19.5 (1-dimensional).

In Figure 44, we depict profiles of the averaged (in radial coordinates of the spherical system) density and pressure of the 3-dimensional liner at stagnation, the density and pressure profiles of a 1-dimensional liner with the same profile as the 3-dimensional liner at the merging radius, and the density and pressure profiles of a 1-dimensional liner with the same mass but sharp profile at the merging radius. We observe that the self-implosion pressure of the 3-dimensional liner, 6.4 kbar, is 10 times smaller compared to the pressure of the equivalent 1-dimensional liner (64 kbar), and 50 times smaller compared to the 1-dimensional liner with the sharp profile at the merging radius (320 kbar). This result contradicts [19] which claims that the self-collapse

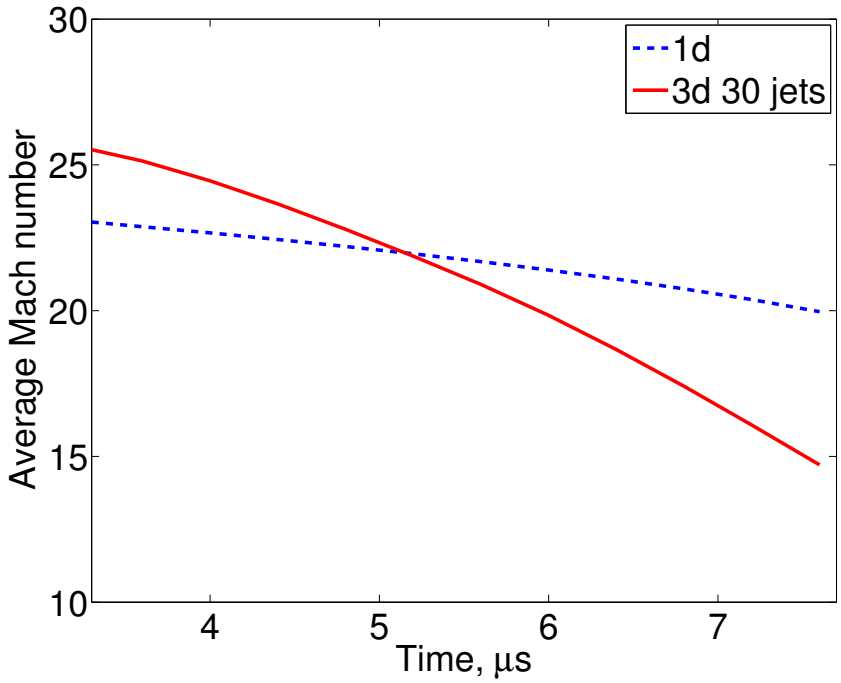

Figure 43: Evolution of average Mach numbers of 1-dimensional and 3-dimensional liners.

pressures of a spherically-symmetric liner and the liner obtained via the merger of plasma jets are approximately equal. In these simulations, we applied the plasma EOS in the vacuum region to mitigate the effect of the residual vacuum gas compressed by the liner. Our studies showed that the energy sinks related to ionization are sufficient for this purpose and artificially high pressures in the vacuum region do not develop. In particular, the use of LTE plasma EOS for the residual gas with the initial pressure of 1 mTorr and the plasma liner with parameters of PLX Table 2, case 6 of [14], increases the self-implosion pressure by 30 times compared to the simulation with polytropic gas EOS for the residual gas. This increase is of the same order as in the case of a complete removal of the vacuum gas. In [14], a mitigation of the vacuum gas influence was obtained by using radiation.

As plasma liners are intended to compress magnetized targets in future experiments, we analyse the uniformity of the converging liner along surfaces parallel to the target surface. Figure 45 shows the distribution of density and pressure on a 10 cm radius spherical slice through the leading edge of the 3-dimensional liner. This plot provides information about the state of the liner before the interaction with a plasma target. We observe that the pressure and density in post-shock regions formed by the three-jet interactions exceed the density and pressure in the main body of jets by approximately 10 times. Such a non-uniformity of liners will have implications for the stability of targets during compression. These processes will be analyzed in a forthcoming paper.

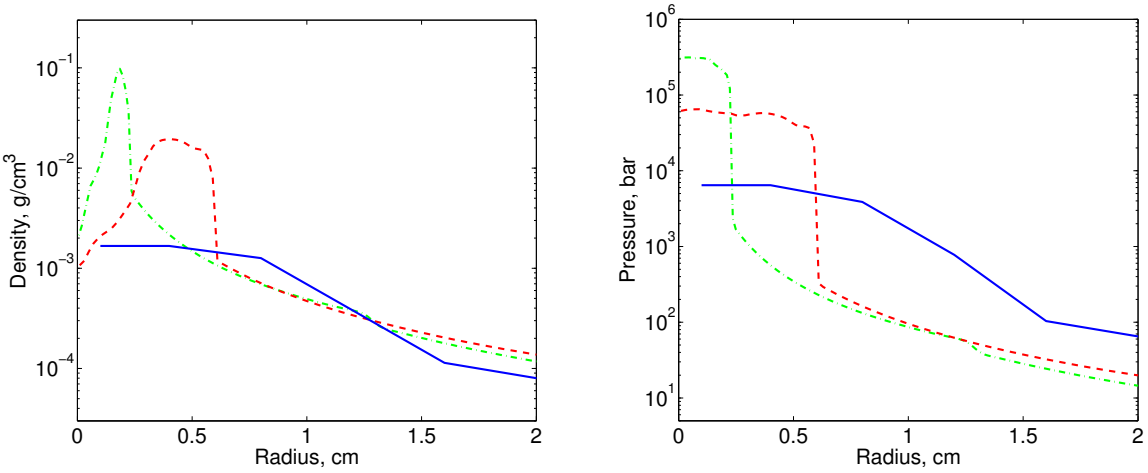

(a) (b)

Figure 44: (Color online) Distribution of density (a) and pressure (b) during stagnation of the 3-dimensional liner averaged in radial coordinates (solid blue line), the 1-dimensional liner initialized with sharp profile at the merging radius (green dash-dotted line) and the 1-dimensional liner initialized with same profile as the 3-dimensional liner at the merging radius (red dashed line).

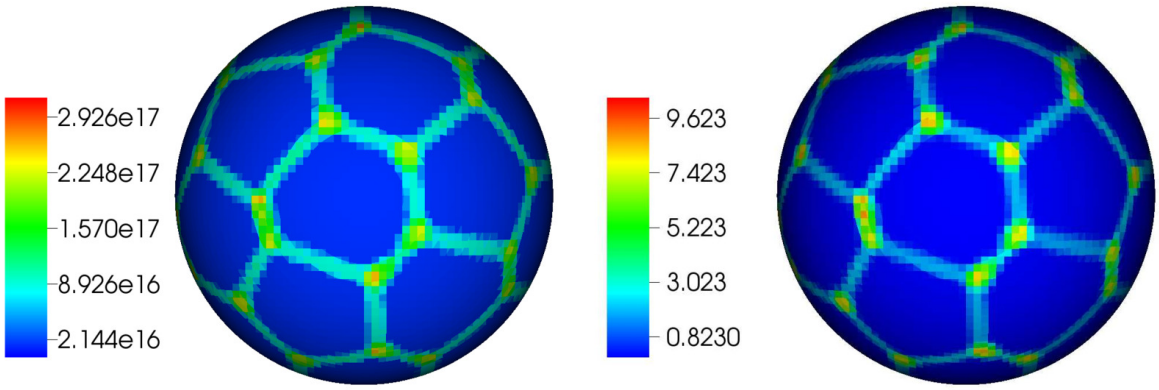

(a) Number density, $1/cm^3$ (b) Pressure, bar

Figure 45: (Color online) Distribution of density and pressure on a 10 cm radius spherical slice of 3-dimensional liner data when t = 0.0253 ms.

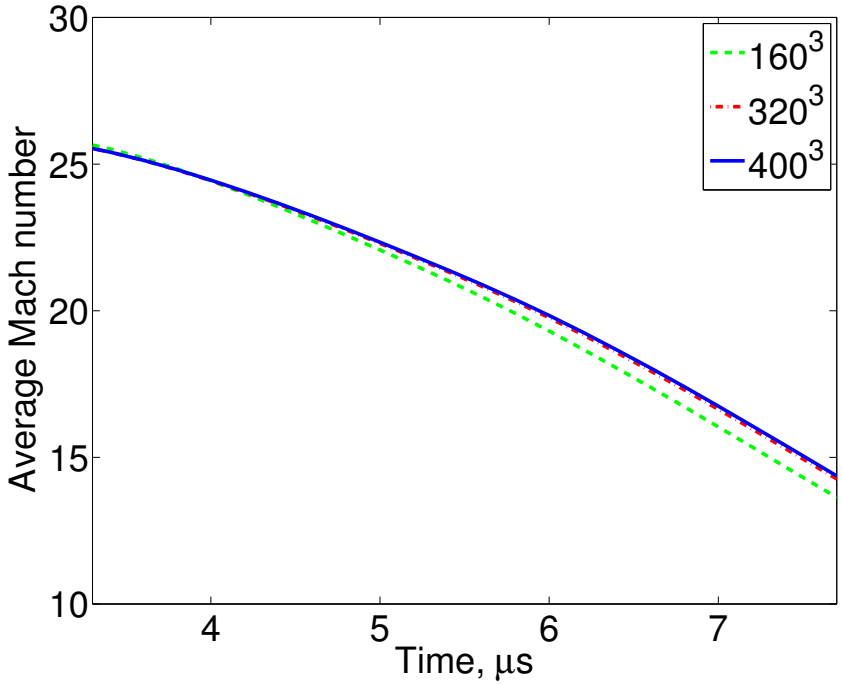

Figure 46: Mesh convergence studies of 3-dimensional liner formation and implosion simulation. Evolution of average Mach number using three different mesh sizes is shown.

Finally, we would like to comment on the numerical resolution and convergence. In the 3-dimensional liner formation and implosion simulation, the domain size is $(160cm)^3$ and the mesh size is $(400)^3$. To ensure numerical accuracy, we have performed the mesh convergence studies. The convergence of the averaged Mach number on meshes with different resolution is shown in Figure 46. The mesh convergence study was performed on even finer meshes using the polytropic EOS, and the results demonstrate that the mesh block size of 0.4 cm is sufficiently accurate for resolving the self-collapse process.

3.5 Summary and Conclusions

A study of the self-implosion and the internal structure of a plasma liner formed by the merger of 30 argon plasma jets relevant to the PLX experiment have been performed via 3-dimensional numerical simulations using the FronTier code. To reduce the computational cost, a cylindrically symmetric 2-dimensional simulation of detached jet from plasma gun was obtained first and simulation results were embedded in a 3-dimensional simulation which had an optimized computational domain. We applied a numerical model for the argon equation of state [2] which captures the ionization of argon atom.

Our study demonstrates that the jet merger process is accomplished via a cascade of oblique shock waves that heat the liner, reduce its Mach number, and lower the self-collapse pressure. To demonstrate the formation of cascades of oblique shock waves in simpler geometry, a 2-

dimensional simulation of the merger of polytropic gas jets was performed and results were compared with the oblique shock theory. We achieved a good agreement with theory on after-shock states of gas after the first and second oblique shocks. The 3-dimensional jets merger process is complicated by (1) secondary shocks due to three-jet interactions, (2) spreading out of free jets in the longitudinal and transverse directions, (3) change of the ionization fraction across the oblique shock wave, and (4) heating associated with the adiabatic compression. We compared the self-implosion density and pressure of the 3-dimensional liner with the pressure and density of 1-dimensional liners with the sharp profile at the merging radius and with profile identical to the average profile of the 3-dimensional liner. We observed that the self-implosion pressure of the 3-dimensional liner, 6.4 kbar, is 10 times smaller compared to the pressure of the equivalent 1-dimensional liner (64 kbar), and 50 times smaller compared to the 1-dimensional liner with the sharp profile at the merging radius (320 kbar). Mesh convergence studies have been performed for all simulations to ensure that results are not affected by the numerical resolution. This result contradicts [19] which claims that the self-collapse pressures of a spherically-symmetric liner and the liner obtained via the merger of plasma jets are approximately equal. The effect of oblique shock waves was studies in this paper using only uniform distribution of 30 jets. If a liner is formed by a larger number of jets, the strength of oblique shock waves will be reduced, but the merging radius and the convergence time of the merged liner will be increased. The number of jets used in this study was dictated by the current experimental equipment and not the liner optimization considerations.

We also observed a large (factor of 10) variations of pressure and density in the leading edge of the liner along spherical surfaces close to the interaction with potential plasma targets. Such a non-uniformity of liners will have implications for the stability of targets during compression. 3-dimensional simulations of the compression of targets by plasma liners using the front tracking numerical method are in progress and results will be reported in a forthcoming paper.

4 3D Simulations of Plasma Targets

4.1 Summary

The compression and stability of plasma targets for the plasma jet-induced magneto-inertial fusion (PJMIF) have been investigated via large scale simulations using the FronTier code capable of explicit tracking of material interfaces. In the PJMIF concept, a plasma liner, formed by the merger of a large number of radial, highly supersonic plasma jets, implodes on a magnetized plasma target and compresses it to conditions of the fusion ignition. A multi-stage computational approach for simulations of the liner-target interaction and the compression of plasma targets has been developed to minimize computing time. Simulations revealed important features of the target compression process, including instability and disintegration of targets. The non-uniformity of the leading edge of the liner, caused by plasma jets as well as oblique shock waves between them, leads to instabilities during the target compression. By using front tracking, the evolution of targets has been studied in 3-dimensional simulations. Optimization studies of target compression with different number of jets have also been performed. This Section os based on [4].

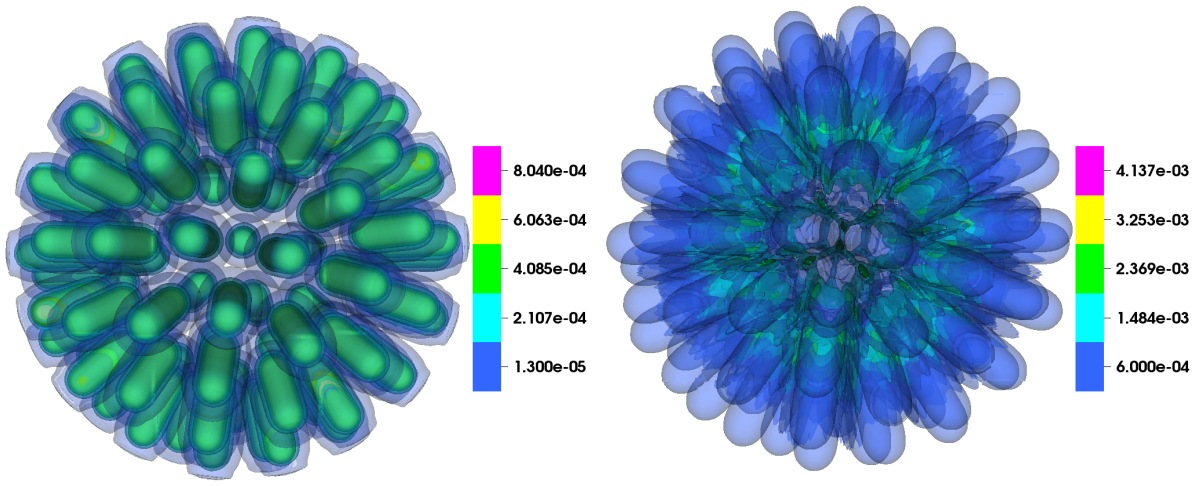

Figure 47: Density contour evolution of the liner formed by 90 jets before interaction with the target at time 0.0097 ms and 0.0123ms.

4.2 Analysis of Simulation Results

First we perform cylindrically-symmetric, 2-dimensional simulation of the propagation of a single detached argon jet from the nozzle of the plasma gun. Here we use the code features that include high-resolution hyperbolic solvers based on the Riemann problem, front tracking, and weakly ionized plasma EOS model with atomic processes. The argon jet has the following initial conditions: the initial inner and outer radii are 137.2 cm and 162.7 cm, respectively, density $\rho = 8.04 \times 10^{-4}\,\mathrm{g/cm^3}$, pressure $P = 18.59\,\mathrm{bar}$, velocity $v = 100\,\mathrm{km/s}$, and Mach number $M = 60$. The ambient vacuum is modeled as rarefied gas with density $\rho_0 \sim 10^{-9}\ g/cm^3$ and pressure $\sim 10^{-6}\ bar$. The computational mesh size is 2 mm. After obtaining the pressure, density, and velocity profiles for the single jet before the merger, we first find directions for 90 jets uniformly distributed in space using Spherical Centroidal Voronoi Tessellation (SCVT), and then initialize states of 90 jets before the merger in a 3-dimensional code. We perform transformation from 2-dimensional cylindrical coordinate into 3-dimensional Cartesian coordinate together with bi-linear interpolation, which initializes the states around each jet direction. The initial mesh size at this stage is 5 mm which we found to be sufficient for the resolution of the jet-merger process. This mesh size is further refined as the simulation progresses. The target is not included in this coarser simulation since we only need the liner information before liner-target interaction. Figures 47 and 48 depict the density and pressure contours before and after the jet merger. Due to oblique shock waves, we observe redistribution of states in the converging liner. At the later stage, the highest pressure and density appear along the plane of interaction of the neighboring jets. This non-uniform distribution causes the instabilities on the target. We also observe the contours with shapes of pentagon and hexagon determined by the location of jets.

Finally, we take the data of the center area from the previous simulation when the liner still remains at some small distance off the target, and re-initialize a refined simulation for the target

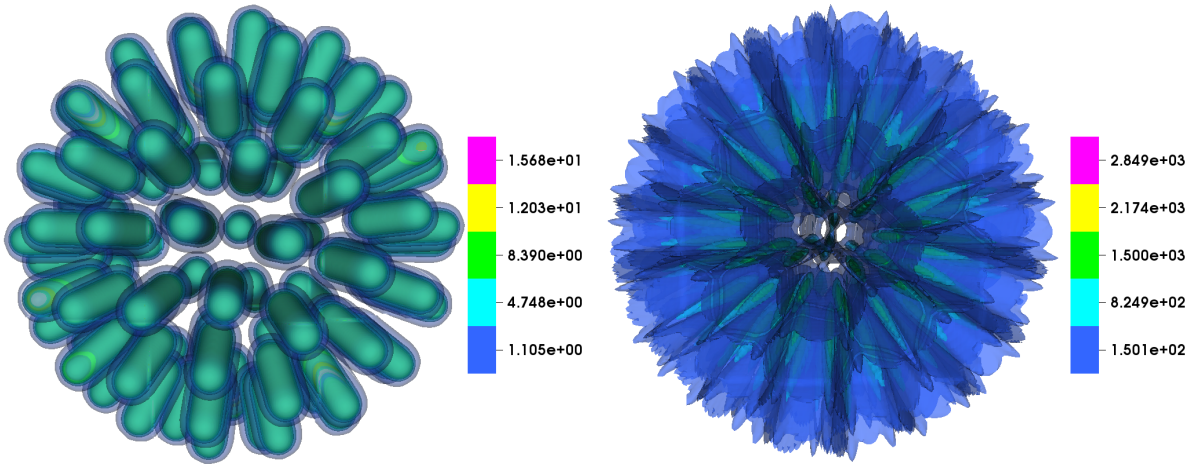

Figure 48: Pressure contour evolution of the liner formed by 90 jets before interaction with the target at time 0.0097 ms and 0.0123ms.

compression study. The target initial condition is as follows: density $\rho = 8.3 \times 10^{-6}\,\mathrm{g/cm^3}$, pressure $P = 640.3\,\mathrm{bar}$. In order to prevent target diffusion, we set the velocity of the target to be zero before the liner-target interaction. As the target is compressed by a non-uniform liner, it develops surface instabilities and even brakes in fragments at the late stage. The target behavior is unstable and complicated after this stage and we currently only focus on the properties of the target before it brakes into fragments. Figure 49 and Figure 50 depict density and pressure contours evolution in the center region including liner and target. Figure 50 shows the interaction between the liner and target with formation of bubbles and spikes on the target at later stage. Here spikes are inward pointing toward the target and bubbles are outward pointing toward the liner. The region with higher density and pressure along the plane of interaction of the neighboring jets compresses the target with higher rate and bubbles and spikes are obtained. The instabilities are amplified with time. In order to inspect the evolution of the target more clearly, we present the evolution of target together with pressure distribution on the interface in Figure 51. The maximum pressure appears on the spikes, in the region of interaction of the neighboring jets which is also the region of the maximum pressure for the liner due to oblique shock waves. The target finally breaks because of this uneven pressure distribution. Figure 52 shows the properties of bubbles and spikes. The bubble and spike heights keep increasing, and the terminal bubble velocity becomes quasi-constant around 12.6 $\mu s \rightarrow 13.1\ \mu s$, before the breakup of the target.

Finally, we perform 1-dimensional spherical symmetric simulation corresponding to a 3-dimensional uniform liner to compare with the full 3-dimensional simulation and quantify the role of non-uniformities and instabilities of the liner and target. The initial conditions, obtained by the averaging of the 3-dimensional data in angular coordinates, are as follows: the inner and outer radii are 137.2 cm and 162.7 cm respectively, the density $\rho = 1.744 \times 10^{-5}\,\mathrm{g/cm^3}$, pressure $P = 0.421\,\mathrm{bar}$, velocity $v = 100\,\mathrm{km/s}$, and Mach number $M = 60$. Figure 53 shows

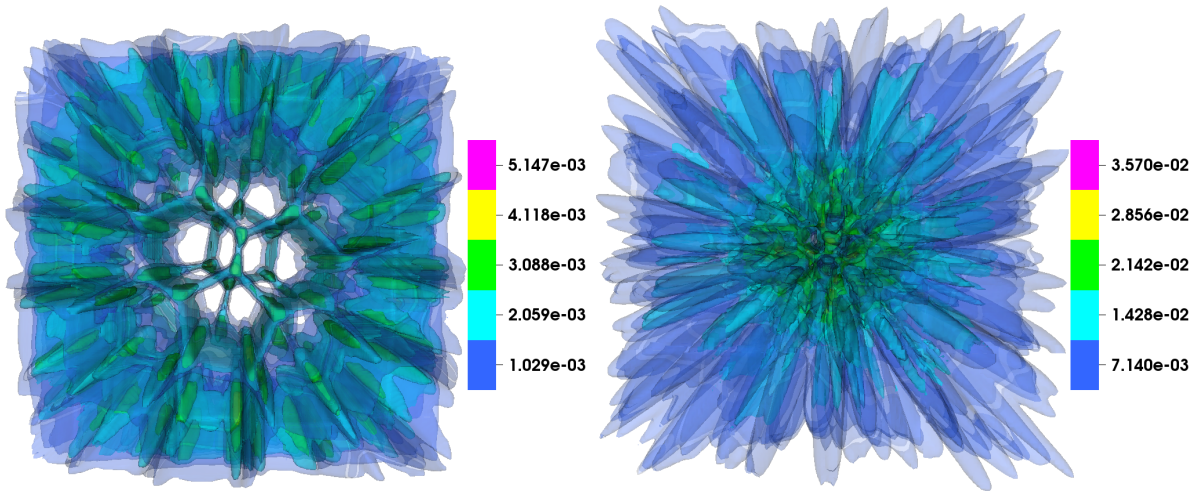

Figure 49: Density contour evolution of the liner and target after their interaction at time 0.0124 ms and 0.0135 ms.

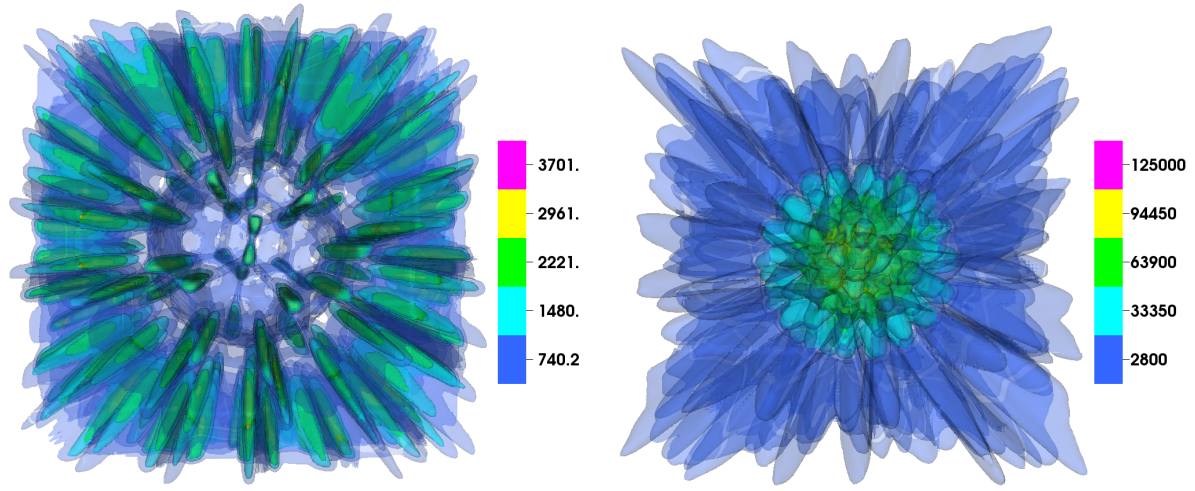

Figure 50: Pressure contour evolution of the liner and the target after interaction at time 0.0124 ms and 0.0135 ms.

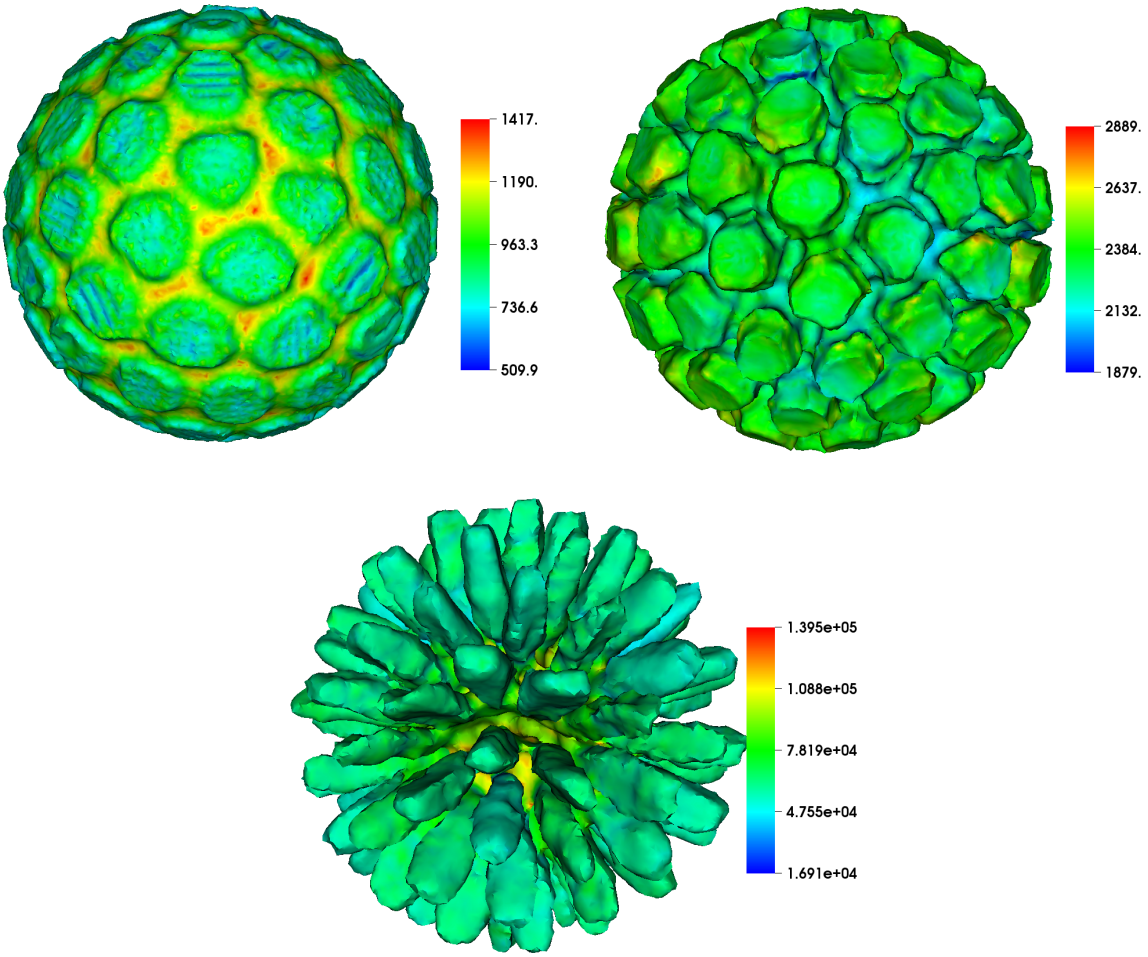

Figure 51: Target evolution together with pressure distributions on the interface at time 0.0124 ms, 0.013 ms and 0.0135 ms.

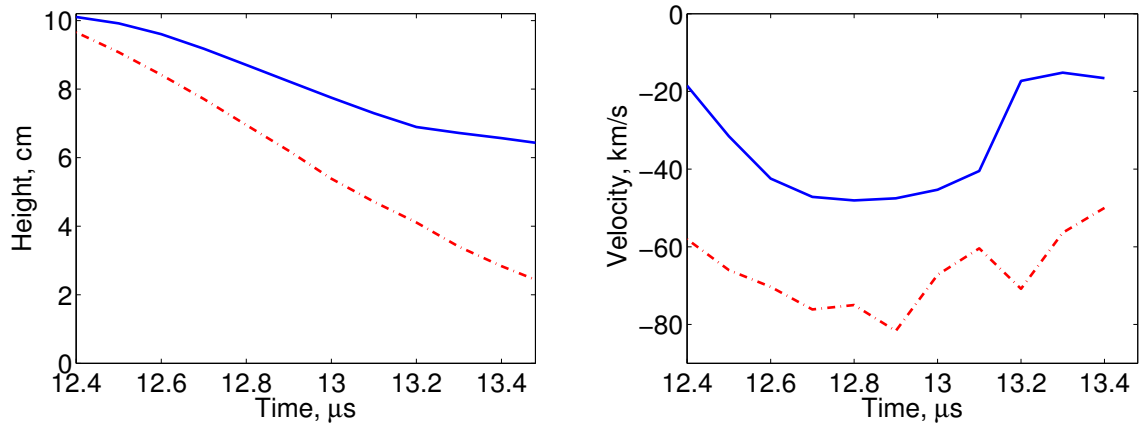

Figure 52: (a) Bubble (blue solid line) and spike (red dashed-dotted line) heights and (b) Bubble (blue solid line) and spike (red dashed-dotted line) velocities evolution from starting of interaction until around target breaking into fragments for 3-dimensional simulation with mesh size as 2 mm based on 5 mm.

the average pressure in the target for different cases. Note that we only focus on the time range of the target compression before fragmentation. The pressures of the 3-dimensinal (90 jets) case and 2-dimensional (16 jets) case are very close to each, around $P = 7.5e4$ bar and $P = 7.1e4$ bar respectively at the end of this time range. The pressure of uniform cases is always higher as expected because of the impact of oblique shock waves for jet case. The 3-dimensinal uniform case (1-dimenstional spherical geometry) is around $P = 6.3 \times 10^6$ bar while the 2-dimensinal uniform case (1-dimenstional cylindrical geometry) is around $P = 1.3 \times 10^6$ bar. The pressure of 3-dimensinal uniform case is almost 80 times higher than that of the 90 jets case. Similar simulations of a self-implosion of liners (without a target) produce the difference of stagnation pressure between a 3-dimensional simulation and the corresponding 1-dimensional uniform problem of about 50 times.

We would like to emphasize that current simulations were performed at conditions compatible with capabilities of the experimental facility at Los Alamos National Laboratory. The achievable pressures and temperatures in targets are well below the fusion ignition. Therefore we do not comment on the fusion energy gain in this work.

4.3 Conclusions

In this paper, we investigated the compression and stability of plasma targets for the plasma jet induced magneto-inertial fusion (PJMIF) via large scale simulations using the FronTier code capable of explicit tracking of material interfaces. A multi-stage computational approach for simulations of the liner-target interaction and the compression of plasma targets has been developed to minimize computing time. Simulations involve the propagation of a single supersonic argon plasma jet, the merger of 90 jets and the formation of a plasma liner, the implosion of the liner, and the compression of a plasma target. Simulation show the formation and evolution

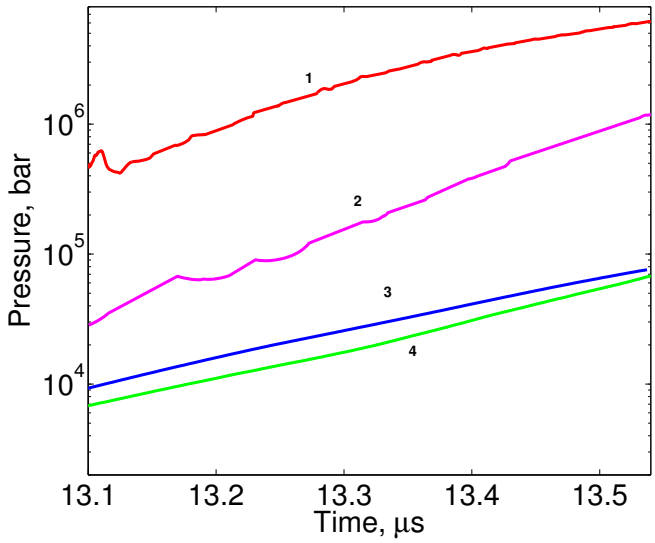

Figure 53: Average pressure in target for (1) 3-dimensional uniform case (1-dimenstional spherical geometry); (2) 2-dimensional uniform case (1-dimenstional cylindrical geometry); (3) 3-dimensional case (90 jets); (4) 2-dimensional case (16 jets).

of oblique shock waves during the jet merger process, consistent with previous studies. These shock waves reduce the average Mach number of the liner and its ability to compress the target, and determine to a large extent the nonuniform properties of the imploding liner. Simulations revealed important features of the target compression process, including instability and disintegration of targets. The non-uniformity of the leading edge of the liner, caused by plasma jets as well as oblique shock waves between them, leads to instabilities during the target compression. Optimization studies of target compression with different number of jets have also been performed.

References

[1] R. Samulyak, P. Parks, L. Wu, Spherically symmetric simulation of plasma liner driven magnetoinertial fusion, Physics of Plasmas, 17 (2010), 092702.

[2] H. Kim, R. Samulyak, L. Zhang, P. Parks, Influence of atomic processes on the implosion of plasma liners, Physics of Plasmas, 19:082711, 2012.

[3] H. Kim, L. Zhang, R. Samulyak, P.Parks, On the structure of plasma liners for plasma jet induced magnetoinertial fusion, Phys. Plasmas 20, 022704 (2013)

[4] S. Samulyak, L. Zhang, H. Kim, On stability of Targets for Plasma Jet Induced Magnetoinertial Fusion, 2015. Submitted

[5] B. Fix, J. Glimm, X. Li, Y. Li, X. Liu, R. Samulyak, and Z. Xu. A TSTT integrated frontier code and its applications in computational fluid physics. *Journal of Physics: Conf. Series*, 16:471–475, 2005.

[6] R. Samulyak, J. Du, J. Glimm, and Z. Xu. A numerical algorithm for MHD of free surface flows at low magnetic reynolds numbers. *J. Comput. Phys.*, 226:1532–1546, 2007.

[7] H.S. Bosch and G.M. Hale, Nucl. Fusion, 1992, Vol. 32, p. 611.

[8] P. B. Parks. On the efficacy of imploding plasma liners for magnetized fusion target compression. *Phys. Plasmas*, 15:062506, 2008.

[9] Y. C. Francis Thio and Ronald. C. Kirkpatrick. Magnetized target fusion driven by plasma liners. In Annual Meeting of the American Nuclear Society, Hollywood, FL, 2002.

[10] J. T. Cassibry, R. J. Cortez, S. C. Hsu, and F. D. Witherspoon. Estimates of confinement time and energy gain for plasma liner driven magnetoinertial fusion using an analytic self-similar converging shock model. *Phys. Plasmas*, 16:112707, 2009.

[11] R. Samulyak, T. Lu, and P. Parks. A hydromagnetic simulation of pellet ablation in electrostatic approximation. *Nuclear Fusion*, 47:103–118, 2007.

[12] Ya. B. Zel'dovich and Yu. P. Raizer. *Physics of shock waves and high-temperature hydrodynamic phenomena*. Dover, 2002.

[13] F. S. Felber, P. B. Parks, R. Prater, and D. F. Vlasow. Effect of atomic processes on fuel pellet ablation in thermonuclear plasma. *Nucl. Fusion*, 19:1061, 1979.

[14] T. J. Awe, C. S. Adams, J. S. Davis, D. S. Hanna, and S. C. Hsu. One-dimensional radiation-hydrodynamic scaling studies of imploding spherical plasma liners. *Phys. Plasmas*, 18:072705, 2011.

[15] H. R. Griem. Validity of local thermal equilibrium in plasma spectroscopy. *Phys. Rev.*, 131:1170 – 1176, 1963.

[16] J.D. Huba, NRL Plasma Formulary, 2011 Edition.

[17] Charles E. Knapp. An implicit smooth particle hydrodynamic code. PhD thesis, Los Alamos national laboratory, 2000.

[18] R. Courant, K.O. Friedrichs. *Supersonic Flow and Shock Waves*, Springer, 1991.

[19] J. T. Cassibry, M. Stanic, S. C. Hsu, S. I. Abarzhi, F. D. Witherspoon. Tendency of spherically imploding plasma liners formed by merging plasma jets to evolve toward spherical symmetry. *Phys. Plasmas*, 19:052702, 2012.